

Thermal non-equilibrium of porous flow in a resting matrix applicable to melt migration: a parametric study

Laure Chevalier, Harro Schmeling

Institute of Geosciences, Goethe University, 60438 Frankfurt, Germany

5 Correspondence to: Harro Schmeling (schmeling@geophysik.uni-frankfurt.de)

Abstract. Fluid flow through rock occurs in many geological settings on different scales, at different temperature conditions and with different flow velocities. Depending on these conditions the fluid will be in local thermal equilibrium with the host rock or not. To explore the physical parameters controlling thermal non-equilibrium the coupled heat equations for fluid and solid phases are formulated for a fluid migrating through a resting porous solid by Darcy flow. By non-dimensionalizing the equations three non-dimensional numbers can be identified controlling thermal non-equilibrium: the Peclet number Pe describing the fluid velocity, the heat transfer number A describing the local interfacial heat transfer from the fluid to the solid, and the porosity ϕ . The equations are solved numerically for the fluid and solid temperature evolution for a simple 1D model setup with constant flow velocity. This setup defines a third non-dimensional number, the model height $H=1/G$, where G is the non-dimensional initial thermal gradient. Three stages are observed: a transient stage followed by a stage with maximum non-equilibrium fluid to solid temperature difference, ΔT_{max} , and a stage approaching the steady state. A simplified time-independent ordinary differential equation for depth-dependent $(T_f - T_s)$ is derived and solved analytically. solved. From these solutions simple scaling laws of the form $(T_f - T_s) = f(Pe, A, \phi, H)$, where H is the non-dimensional model height, (Pe, G, z) are derived. Due to scaling they don't depend explicitly on ϕ anymore. The solutions for ΔT_{max} and the scaling laws are in good agreement with the numerical solutions. The parameter space Pe, A, ϕ, HG is systematically explored. In the $Pe - A$ parameter space three Three regimes can be identified: 1) at high Pe ($>1/G$) strong thermal non-equilibrium develops independently of Pe and A ; 2) at low Pe (<1) and low A ($<1/G$) non-equilibrium decreases proportional to decreasing $Pe \cdot A$; 3) at low Pe (<1) and large A (>1) non-equilibrium scales with Pe/A and thus becomes unimportant. G of order 1 the scaling law is $\Delta T_{max} \approx Pe$. The porosity ϕ has only a minor effect. scaling laws are also given in dimensional form. The dimensional ΔT_{max} depends on thermal non-equilibrium the initial temperature gradient, the flow velocity, the melt fraction, the interfacial boundary layer thickness, and the interfacial area density. The time scales for reaching thermal non-equilibrium scale with the advective time-scale in the high Pe -regime and with the interfacial diffusion time in the other two low Pe -regimes. Applying the results to natural magmatic systems such as mid-ocean ridges can be done by estimating appropriate orders of Pe and AG . Plotting such typical ranges in the $Pe - A - G$ regime diagram reveals that a) interstitial melt flow is in thermal equilibrium, b) melt channelling such as e.g. revealed by dunite channels may reach moderate thermal non-equilibrium, and c) the dyke regime is at full thermal non-equilibrium.

Formatiert: Schriftart: Kursiv

Formatiert: Schriftart: Kursiv

1 Introduction

Fluid flow through rock occurs in many geological settings on different scales, at different temperature conditions and with different flow velocities. Depending on these conditions the fluid will be in local thermal equilibrium with the host rock or not. On small scale, e.g. grain scale, usually thermal equilibrium is valid. Examples include melt migration through a porous matrix in the asthenosphere or in crustal magmatic systems at super-solidus temperatures (e.g. McKenzie, 1984), groundwater or geothermal flows in sediments or cracked rocks (e.g. Verruijt, 1982; Furbish, 1997; Woods, 2015), or hydrothermal convection in the oceanic crust (e.g. Davis et al., 1999; Harris and Chapman, 2004; Becker and Davies, 2004). On a somewhat larger scale local thermal equilibrium may not always be reached. Examples of such flows include melt migration in the mantle or crust at temperatures close to or slightly below the solidus where melt may be focused and migrates through systems of veins or channels (Kelemen et al., 1995; Spiegelman et al., 2001). Within the upper oceanic crust also water may migrate through systems of vents or channels (Wilcock and Fisher, 2004). At even larger scales and at sub-solidus conditions magma rapidly flows through propagating dykes or volcanic conduits (e.g. Lister and Kerr, 1991; Rubin, 1995; Rivalta et al., 2015) and is locally at non-equilibrium with the host rock.

Heat transport associated with most of such flow scenarios is usually described by ~~either~~ assuming thermal equilibrium between the fluid and solid ~~in case of under~~ slow flow ~~velocity conditions~~ (e.g. McKenzie 1984) ~~or~~. Alternatively, for more rapid flows such melts moving in dykes through a cold elastic or visco-elasto-plastic ambient rock, ~~by assuming~~ the fluids are assumed as isothermal (e.g. Maccaferri et al., 2011; Keller et al., 2013). However, on local scale of channel or dyke width thermal interaction between rising hot magma and cold host rock is important and may lead to effects such as melting of the host rock and freezing of the magma with important consequences for dyke propagation and the maximum ascent height (e.g. Bruce and Huppert, 1990; Lister and Kerr, 1991; Rubin, 1995). Clearly, in such rapid fluid flow scenarios melt is not in thermal equilibrium with the ambient rock.

Thus, there exists a transitional regime, which, for example, may be associated with melt focusing into pathways where flow is faster and thermal equilibrium might not be valid anymore. In such a scenario it might be possible that channelized flow of melt might penetrate deeply into sub-solidus ambient rock, and thermal non-equilibrium delays freezing of the ascending melts and promotes initiation of further dyke-like pathways. Indeed, for mid-oceanic ridges compositional non-equilibrium has proven to be of great importance for understanding melt migration and transport evolution (Aharonov et al., 1995; Spiegelman et al., 2001). Thus, it appears plausible that in cases of sufficiently rapid fluid flow e.g. due to channeling or fracturing thermal non-equilibrium may also become important. Describing this non-equilibrium macroscopically, i.e. on a scale larger than the pores or channels, is the scope of this paper.

While the physics of thermal non-equilibrium in porous flow is well studied in more technical literature (e.g. Spiga and Spiga, 1981; Kuznetsov, 1994; Amiri and Vafai, 1994; Minkowycz et al., 1999; Nield and Bejan, 2006; de Lemos, 2016), so far it

has attracted only little attention in the geoscience literature, but see Schmeling et al., (2018) and Roy (2020). The basic approach in all these studies is the decomposition of the heat equation for porous flow into two equations, one for the solid and one for the migrating fluid. The key parameter for thermal non-equilibrium is a heat exchange term between fluid and solid, which appears as a sink in the equation for the fluid and as a source in the equation for the solid. Usually, this heat exchange term is assumed proportional to the local temperature difference between fluid and solid (Minkowycz et al. 1999; Amiri and Vafai, 1994; de Lemos, 2016; Roy, 2020), ~~although~~. However, Schmeling et al. (2018) showed that in a more general formulation the heat exchange term depends on the complete thermal history of the moving fluid through the possibly also moving solid. Here we will follow the common assumption and use the local temperature difference formulation. While Schmeling et al. (2018) showed that the magnitude of thermal non-equilibrium essentially depends on the flow velocity, or more general, on the Peclet number, here we will more generally explore the parameter space.

While thermal non-equilibrium of an arbitrary porous flow system depends on many parameters, our approach is to reduce the complexity of the system and systematically explore the non-dimensional parameter space. It will be shown that only ~~three~~ two non-dimensional parameters control thermal non-equilibrium in porous flow, namely the Peclet number, ~~an interfacial heat exchange number~~, and the porosity. In our simple 1D model setup with constant flow velocity a third non-dimensional number, the model height $H=1/G$, where G is the non-dimensional initial thermal gradient is identified. The non-dimensionalization allows application of the results to arbitrary magmatic or other systems. The aim is to derive scaling laws ~~allowing easily to decide~~ that allow an easy determination of whether thermal equilibrium or non-equilibrium is to be expected and quantitatively to estimate the maximum temperature difference between fluid and matrix. The results will be applied to an anastomosing melt ascent system typical for mid-oceanic ridges in a second paper (Chevalier and Schmeling, in prep).

2 Governing equations and model setup

2.1 Heat conservation equations

We ~~consider start with considering~~ a homogeneous general two-phase matrix-fluid system with ~~a porosity constant in space variable properties and time. We assume a constant solid and fluid velocity velocities and subsequently apply simplifications.~~ The two phases are incompressible, and we assume local thermal non-equilibrium conditions, i.e. the two phases exchange heat. ~~We solve the~~ The equations for conservation of energy ~~(de Lemos, 2016) in of~~ this system. ~~Conservation are given e.g. by de Lemos (2016). Assuming constant pressure the conservation~~ of energy of the fluid phase is given by:

$$c_{p,f} \left(\frac{\partial(\phi \rho_f T_f)}{\partial t} + \nabla \cdot (\phi \rho_f v_f T_f) \right) = \nabla \cdot (\phi \lambda_f \nabla T_f) - Q_{fs} \quad (1)$$

For the definition of all quantities, see Table 1. Equation (1) can be ~~further developed~~ rearranged into:

$$c_{p,f} \left(T_f \frac{\partial(\phi \rho_f)}{\partial t} + \phi \rho_f \frac{\partial T_f}{\partial t} + T_f \nabla \cdot (\phi \rho_f v_f) + \phi \rho_f v_f \cdot \nabla T_f \right) = \nabla \cdot (\phi \lambda_f \nabla T_f) - Q_{fs} \quad (2)$$

Mass conservation for the fluid phase is given by:

$$\frac{\partial(\rho_f \phi)}{\partial t} + \nabla \cdot (\rho_f \phi v_f) = 0 \quad (3)$$

95 Inserting (3) into (2), conservation of energy for the fluid phase ~~resumes to becomes~~:

$$c_{p,f} \rho_f \phi \left(\frac{\partial T_f}{\partial t} + v_f \cdot \nabla T_f \right) = \nabla \cdot (\phi \lambda_f \nabla T_f) - Q_{fs} \quad (4)$$

In a similar way, the conservation of energy of the solid phase is given by:

$$c_{p,s} \rho_s (1 - \phi) \left(\frac{\partial T_s}{\partial t} + v_s \cdot \nabla T_s \right) = \nabla \cdot ((1 - \phi) \lambda_s \nabla T_s) + Q_{fs} \quad (5)$$

which, assuming that $v_s = 0$, is further simplified:

$$110 \quad c_{p,s} \rho_s (1 - \phi) \frac{\partial T_s}{\partial t} = \nabla \cdot ((1 - \phi) \lambda_s \nabla T_s) + Q_{fs} \quad (6)$$

The term Q_{fs} in the fluid and solid heat conservation equations is the interfacial heat exchange term between the two phases (fluid and solid). In general, it depends on the local thermal history of the two phases and the history of the heat exchange (Schmeling et al., 2018). In a simplification it can be written as a combination of the interfacial area density S , the interfacial boundary layer thickness δ , the effective thermal conductivity λ_{eff} and the temperatures of the two phases:

$$105 \quad Q_{fs} = \frac{S \lambda_{eff}}{\delta} (T_f - T_s) \quad (7)$$

In general, the term δ is time dependent. Schmeling et al. (2018) however provide evidence that taking an appropriate constant value for δ (depending on fluid velocity) gives a good approximation of Q_{fs} and allows for a reasonable modeling of temperature evolution with time. In most of the following parametric study, we use this simplification for δ by assuming it is constant with time. ~~The influence of time dependence is discussed in section 5.1.4.~~

110

2.2 Scaling and non-dimensionalization

Non-dimensionalization is useful for interpreting models involving a large number of parameters. It usually helps reducing the number of parameters, and identifies non-dimensional parameters that control the evolution of the system. We write the two energy conservation equations in a non-dimensional form, using

$$115 \quad T = \Delta T_0 T', \quad t = t_0 t', \quad v = \frac{\nu_0}{\nu_0} v', \quad (x, y, z) = \frac{L_0}{L_0} (x', y', z') \quad (8)$$

where ΔT_0 is the macroscopic scaling temperature difference of the system, i.e. the initial temperature difference between top and bottom, ν_0 is a distance, ν_0 is the scaling fluid velocity, x, y, z is a distance, L_0 is the scaling length ~~chosen as channel width of the pores, and~~

$$120 \quad L = \sqrt{\frac{\phi_0(1-\phi_0)\delta}{S}} \quad (9)$$

with ϕ_0 as a scaling porosity, and $t_0 = \frac{L_0^2}{\kappa_B A}$

(9a)

is the scaling time, ~~where~~

Formatiert: Schriftart: Kursiv

$$A = S' / (\phi_0 dm') \quad \text{based on} \quad (10a)$$

is defined as the heat transfer number-diffusion time over the length L ,

$$t_0 = L^2 / \kappa_0 \quad (10)$$

(see Table 1 for definitions). Primed quantities are non-dimensional. The scaling time and A can also be written as Introducing the fluid filled pore width d_f and the solid (grain) width d_s , the interfacial area density S scales with

$$t_0 = L_0^2 dm' / (c \kappa_0) \quad (9b)$$

and

$$A = c L_0 / dm' = c / dm' \quad (10b)$$

$$\text{where } S = \frac{c \phi_0}{d_f} \quad (11)$$

for melt channels, tubes, pockets for all melt fractions, and for melt films at small melt fractions, while S scales with

$$S = \frac{c_s (1 - \phi_0)}{d_s} \quad (12)$$

for melt channels, films and suspensions at all melt fractions. Here c is a geometrical constant of the order 2 for melt channels or, 4 for tubes-melt tubes, 6 for melt pockets, and 2 for melt films at small melt fractions. The geometrical constant c_s is of order 2 for melt channels, and 6 for melt films or suspensions. Thus, the scaling time and scaling length can also be written as

$$t_0 = \frac{(1 - \phi_0) d_f \delta}{c \kappa_0} = \frac{\phi_0 d_s \delta}{c_s \kappa_0} \quad (10a)$$

and

$$L = \sqrt{\frac{(1 - \phi_0) \delta d_f}{c}} = \sqrt{\frac{\phi_0 \delta d_s}{c_s}} \quad (9a)$$

Eq. (9a) shows that L scales both with the geometric mean of the channel width, L_0 , and interfacial boundary layer thickness, dm . The non-dimensional heat transfer number A scales with the ratio of the pore dimension to the interfacial boundary layer thickness, or directly d_f and δ at small melt fractions, and with the inverse non-dimensional boundary layer thickness-geometric mean of d_s and δ at large melt fractions. Thus, L is a natural length scale associated with thermal equilibrium of fluid filled pores. The above scaling laws for S justify using the term $\phi_0 (1 - \phi_0)$ in the scaling length L .

Besides, we consider We assume that the fluid and solid phases have the same densities and thermal properties: (but relax this assumption later in section 5.1.3):

$$c_{p,f} = c_{p,s} = c_{p,0}, \quad \rho_f = \rho_s = \rho_0, \quad \kappa_f = \kappa_s = \frac{\lambda_{eff}}{c_{p,0} \rho_0} = \kappa_0 \quad (11)$$

This assumption is discussed in section 5.1.3.

From Eq. (4), (6), and (7) we get the non-dimensional energy conservation equations for the fluid and solid phases, respectively:

Formatiert: Schriftart: Kursiv

$$\frac{\partial T_f'}{\partial t'} + \frac{\rho_0}{A} v_f' \cdot \nabla T_f' = \frac{1}{\phi A} \phi \left(\frac{\partial T_f'}{\partial t'} + Pe v_f' \cdot \nabla T_f' \right) = \nabla \cdot (\phi \nabla T_f') - \frac{\phi_0}{\phi} (T_f' - T_s') \phi_0 (1 - \phi_0) (T_f' - T_s')$$

(12)(14)

$$\frac{\partial T_s'}{\partial t'} (1 - \phi) \frac{\partial T_s'}{\partial t'} = \frac{1}{(1 - \phi) A} \nabla \cdot ((1 - \phi) \nabla T_s') + \frac{\phi_0}{(1 - \phi)} \phi_0 (1 - \phi_0) (T_f' - T_s')$$

(13)(15)

From these equations we notice that the thermal evolution of the two-phase system is controlled by three two non-dimensional parameters: Pe , A , and numbers: the scaling porosity ϕ_0 where and the Peclet number Pe defined as

$$Pe = \frac{v_f \phi_0 L}{\kappa_0} \quad (14)$$

is the Peclet number. $Pe = \frac{v_f \phi_0 L}{\kappa_0}$

(16)

This number has already proven to be of high significance for determining whether thermal non-equilibrium is present or not (Schmelting et al. 2018), and the highest Pe corresponds to the largest temperature difference between fluid and matrix. In the following we drop the primes keeping all equations non-dimensional, only if non dimensionality is to emphasized, primes will be used if not indicated otherwise.

From Eq. (12) and (13) two other controlling parameters can be identified: The heat transfer number A characterizes heat transfer efficiency at the fluid-matrix interface. The larger A , the easier it is to transfer heat as A scales directly with the inverse non-dimensional boundary layer thickness. The last controlling parameter is ϕ_0 , the scaling porosity.

In the following we will consider only models a homogeneous two-phase matrix-fluid system in 1D, with a porosity constant porosity in space and time, i.e. $\phi = \phi_0$ and with. We assume a constant fluid velocity. The latter which will be expressed in terms of Pe , thus we choose $v_f' = \text{the non-dimensional velocity } v_f = 1$. This simplifies equations (12)(14) and (13)(15) to

$$\frac{\partial T_f}{\partial t} + \frac{\rho_0}{A} \frac{\partial T_f}{\partial z} = \frac{1}{A} \frac{\partial^2 T_f}{\partial z^2} - (T_f - T_s)$$

(15) $Pe \frac{\partial T_f}{\partial z} = \frac{\partial^2 T_f}{\partial z^2} - (1 - \phi_0)(T_f - T_s)$

(17)

and

$$\frac{\partial T_s}{\partial t} = \frac{\partial^2 T_s}{\partial z^2} + \phi_0 (T_f - T_s), \quad (18)$$

respectively. As we are interested in the evolution of the non-equilibrium temperature difference between the solid and fluid, subtraction of Eq. (18) from Eq. (17) gives:

$$\frac{\partial (T_f - T_s)}{\partial t} - \frac{\partial^2 (T_f - T_s)}{\partial z^2} + Pe \frac{\partial T_f}{\partial z} + (T_f - T_s) = 0 \quad (19)$$

which is equivalent to:

$$\frac{\partial T_s}{\partial t} = \frac{1}{A} \frac{\partial^2 T_s}{\partial z^2} + \frac{\phi_0}{(1 - \phi_0)} (T_f - T_s), \quad (16)$$

Formatiert: Schriftart: Kursiv

Formatiert: Schriftart: Kursiv

Formatiert: Schriftart: Kursiv

$$\frac{\partial(T_f - T_s)}{\partial t} - \frac{\partial^2(T_f - T_s)}{\partial z^2} + Pe \frac{\partial(T_f - T_s)}{\partial z} + (T_f - T_s) = -Pe \frac{\partial T_s}{\partial z} \quad (20)$$

Note that while the temperatures T_f and T_s explicitly depend on two non-dimensional numbers Pe and ϕ_0 , the temporal evolution of the temperature difference $(T_f - T_s)$ explicitly depends only on Pe . However, implicitly it is still a function of ϕ_0 because T_s on the right-hand-side of Eq. (20) depends on ϕ_0 via Eq. (18). Only for cases or stages with T_s independent of ϕ_0 as proposed in section 4, the temperature difference $(T_f - T_s)$ is a function of only one non-dimensional parameter, Pe , and no more of ϕ_0 .

respectively.

2.3 Model setup

The fluid and solid heat conservation equations are solved in ~~1D~~ a 1D domain of height H . Other geometries could also be easily explored but are not considered here, since we focus on studying the relative control of the scaling parameters on thermal non-equilibrium evolution. At time $t < 0$, both solid and liquid are at rest, in equilibrium. For both phases temperatures are set to 1 (non-dimensional temperature difference) at $z=0$, and a constant flux condition $\partial T / \partial z = 1/H$ (non-dimensional) is imposed at $z=H$. fluid are at rest, in equilibrium. Both initial temperatures decrease linearly from 1 to 0 with z , therefore a constant temperature gradient of $1/H$ is present in both phases (see Fig. 1). $-G = -1/H$ is present in both phases (see Fig. 1). As boundary condition both phases temperatures are set to 1 (non-dimensional temperature difference) at $z = 0$. At $z = H$ a constant thermal gradient condition $\partial T / \partial z = -1/H$ (non-dimensional) is imposed for both phases. At $z = 0$ the advective flux is fixed by the constant temperature condition, i.e. it is equal to $Pe \phi_0$, while at $z = H$ it evolves freely with the fluid temperature, i.e. it is given by $T_f Pe \phi_0$ (all non-dimensional). This top boundary condition needs some justification: The hyperbolic partial differential equations Eq. (17) or (18) require two well defined boundary conditions each, Dirichlet (fixed temperature), Neumann (fixed thermal gradient), Robin (fixed sum of advective and conductive heat flux) or Cauchy (fixed temperature and thermal gradient). Applying the Dirichlet condition at the bottom, leaves either a Dirichlet, a Neumann or a Robin condition to specify for the top. In an open outflow situation like our system neither the evolution of the temperature, the thermal gradient or the total (advective plus conductive) heat flux is known a priori, but depends on the evolution within the system. In the early stage of model evolution both the solid and fluid have a thermal gradient inherited from the initial condition which is advected upwards in the fluid. Thus it seems most appropriate to use the Neumann condition as a boundary condition. Only at later stages this boundary condition imposes artefacts in the temperatures field close to the top boundary. The limitations of this top boundary condition are tested and discussed in chapter 5.1.2. This model setup adds a third non-dimensional scaling parameter to the system, namely $G = 1/H$. It defines the initial non-dimensional temperature gradient or conductive heat flux, positive for a flux directed upwards. To summarize, the temperatures depend on the non-dimensional parameters Pe , ϕ_0 , and G .

2.3.4 Numerical scheme

The equations are solved with a MATLAB (MATLAB R2018b-R2021b) code using a finite difference scheme central in space for the conduction terms, upwind for the advection term, and explicit in time. The spatial resolution is $\Delta z = H/40000$, and the time resolution was varied depending on the studied case $\Delta t = 0.1$ or $\min(0.1, H/100)$ for $H < 10$. The time step was chosen as $\Delta t = \frac{1}{4} \min(\Delta z / Pe, \Delta z^2)$, i.e. taking the minimum of the Courant or diffusion criterion. Tests with smaller spatial and temporal resolution have been carried out and did not change the results visibly.

3 Numerical model results

First, some exemplary numerical results are shown in Fig. 2 to understand the physics and the typical behavior.

3.1 Evolution of temperatures and thermal non-equilibrium with time

Three different models have been run, all with $Pe = 1$ and the following other parameters: Model 1: $H = 10, \phi = 0.1$, model 2: $H = 100, \phi = 0.1$, and Model 3: $H = 100, \phi = 0.2$. Figure 2a and b represent T_f and T_s as functions of z at different times as indicated for two different models. In both models, $Pe = 1, A = 1, \phi = 0.1$. However, while in the first model (Fig. 2a) $H = 10$, in the second one (Fig. 2b) $H = 100$. Initial temperature gradients, $G = 0.1$ ($H = 10$) and $G = 0.01$ ($H = 100$), respectively. Figure 2c shows the evolution of T_f and T_s with time at the top of the domain, for the same model 2 as in Figure 2b, and for model 3 with a higher melt fraction $\phi = 0.2$. Figure 2d represents the evolution of $(T_f - T_s)$ at different distances z in model 2 (Fig. 2b).

At each depth of the system, the fluid and solid temperatures, as well as the temperature difference, appear to evolve following three stages:

Stage 1: During this transient stage the fluid temperature increases faster than the solid temperature (Fig. 2a,b,c,e), and the temperature difference (Fig. 2d,f) increases. During this stage, the fluid temperature increases rapidly at first, then the temperature increase slows down. As for the solid temperature, it first increases slowly, then faster and faster. At $t = 0$, the fluid velocity is suddenly set to non-zero, thus the fluid temperature starts to deviate from equilibrium and increases in agreement with these new conditions. If the solid temperature were maintained constant with time, the fluid temperature would probably reach a steady-state profile, depending on boundary conditions, fluid velocity and solid temperature. As while the fluid temperature increases however, faster than the liquid solid temperature, the fluid-solid temperature difference, thus the heat transfer term, increases too, making forcing the solid temperature to progressively increase also faster and faster. At the end of stage 1 the maximum temperature difference is approached (Fig. 2f). Because the solid temperature hasn't risen significantly at that time (at $t = 4$ in the example) compared to the fluid temperature (Fig. 2e) different melt fractions do not affect the temperature differences during this stage (Fig. 2f in which all curves merge in one curve). This observation confirms the expectation from Eq. (20) that the temperature difference does not depend on melt fraction as long as the solid temperature is independent of ϕ , which is the case as long as T_s stays close to its initial profile.

Formatiert: Schriftfarbe: Rot

245 **Stage 2:** The fluid and the solid temperatures increase at similar rates, constant with time (Fig. 2c), the temperature difference remains stable (Fig. 2d). Solid-fluid heat transfer is maximum here, constant and at maximum at the top (Fig. 2d). Solid-fluid heat transfer is at maximum during this stage. As T_s is no more constant in time, different melt fractions lead to different rates of temperature increase (Fig. 2c) and also to different evolutions of $(T_f - T_s)$ (Fig. 2d solid curves compared to dashed curves). A higher melt fraction increases the heat transfer into the solid (c.f. last term in Eq. 18), resulting in a faster increase of the solid temperature whose gradient flattens earlier. Thus, the end of stage 2 is reached earlier (Fig. 2b).

250 **Stage 3:** As the fluid temperature rises close to the T_f value at the bottom, its increase slows down, and heat transfer, thus temperature difference, decreases. In model 1 (Fig. 2a), steady state is reached while the fluid and solid temperatures are still far from 1. This is due to the influence of boundary conditions, as the heat transferred from the fluid phase to the solid phase is compensated by the solid phase heat loss of heat at the top of the domain. In model 2 (Fig. 2b), boundary conditions at $z =$
255 H are applied farther away from the bottom, therefore allowing for a higher increase of temperatures when reaching the steady state.

At each z we observe that the temperature difference first increases rapidly to reach a maximum after a short time (stage 1), here after $t = 24$ (Fig. 2f). The resulting amplitude of the temperature difference is identical at the different z -positions; and for both melt fractions. Then it stays constant at this maximum value (stage 2), and finally decreases (stage 3) (Fig. 2d), as the fluid and solid temperatures experience the different stages. The higher in the model, the longer the temperature difference remains at maximum. This A higher melt fraction accelerates the decrease of $(T_f - T_s)$. The absolute maximum temperature difference in space and time does not depend on boundary conditions (see also section 5.1.2 where the influence of boundary conditions is discussed), nor on the z -position nor on the melt fraction and therefore looks to be an interesting observable. It could indeed be useful for getting a first order estimate of thermal non-equilibrium conditions and possible temperature difference in a magmatic system. In the following sections we study how this maximum temperature difference evolves when varying the three parameters Pe , A and ϕ parameter Pe .

3.2 Maximum temperature difference

The maximum temperature difference of a model can be defined as the maximum value reached in space and time (c.f. Fig. 2d). A series of models has been carried out for the two different non-dimensional parameters Pe , A , and $G = 1 - \phi$ (= solid fraction), H , and ΔT_{max} has been determined for each model (Fig. 3). Some first observations can be made:-

- For high Pe and high A , ΔT_{max} is proportional to Pe/A (Fig. 3a) as long as ΔT_{max} is somewhat smaller than the absolutely possible maximum 1.
- For small Pe , values align on a linear trend, proportional to Pe and independent of A (Fig. 3a).
- The value of A determines two main regimes, one in which is asymptotically approached for high Pe .
- ΔT_{max} is proportional to Pe/AG , i.e. to the non-dimensional temperature gradient for $G < 0.1$.

275

Formatiert: Schriftfarbe: Rot

Formatiert: Schriftfarbe: Rot

Formatiert: Schriftart: Kursiv

Formatiert: Nicht Hochgestellt/ Tiefgestellt

Formatiert: Schriftart: Kursiv

- ΔT_{max} reaches a maximum for large G of order 1, i.e. when A is high (Fig. 3b), and one in which H reaches 1 or the dimensional H reaches the scale L .
- ΔT_{max} is proportional to Pe when A is small (Fig. 3a) and essentially independent of ϕ as models with different ϕ almost merge in the same points shown in Fig. 3. This has been verified by running all models of Fig. 3 with melt fractions between 0.1 and 0.9 (not shown).
- ΔT_{max} is proportional to $(1 - \phi)$ for $Pe = A$ larger than 0.1 (Fig. 3c).

These observations suggest the existence of several domains in which scaling laws for ΔT_{max} could be derived, based on the ~~three~~two scaling parameters. In the next section, we propose an analytical ~~retrieval~~derivation of ΔT_{max} values to ~~derive~~ ~~these~~obtain scaling laws and confirm ~~these observations~~the observed proportionalities.

4 Scaling laws derived from analytical solution

In this section a simplified analytical solution for the z -dependent temperature difference between fluid and solid will be derived. From this ~~solution~~solution the maximum temperature differences ΔT_{max} can be ~~retrieved~~obtained and scaling laws will be derived.

4.1 Analytical solution of the governing equations

The subtraction of Eq. (16) from Eq. (15) gives the following non-dimensional 1D equation. We are interested in an analytical solution of the equation (20) controlling the non-equilibrium temperature difference $(T_f - T_s)$.

$$\frac{\partial(T_f - T_s)}{\partial t} + \frac{1}{A} \frac{\partial^2(T_f - T_s)}{\partial x^2} + \frac{Pe}{A} \frac{\partial(T_f - T_s)}{\partial z} + \frac{1}{1 - \phi} (T_f - T_s) = 0 \quad (17)$$

which is equivalent to:

$$\frac{\partial(T_f - T_s)}{\partial t} + \frac{1}{A} \frac{\partial^2(T_f - T_s)}{\partial x^2} + \frac{Pe}{A} \frac{\partial(T_f - T_s)}{\partial z} + \frac{1}{1 - \phi} (T_f - T_s) = -\frac{Pe}{A} \frac{\partial T_s}{\partial z} \quad (18)$$

Remember that $\phi = \phi_0$ is assumed constant. We simplify the problem by considering the hypothetical case in which $(T_f - T_s)$ does not change with time, and, moreover, in which the thermal gradient in the solid phase is ~~fixed and~~ linear, with $\partial T_s / \partial z = -G = -1/H$ (non-dimensional, with dimensions: $G = \Delta T / H \cdot T_0 / H$). Although different from initial and steady-state stages described in the 1D models (section 3.1), this hypothetical case is quite similar to what can be observed at the very beginning of the second stage described in section 3.1 (c.f. Fig. 2d,f). In this second stage, the evolution of T_f and T_s was ~~indeed~~observed to ~~be being~~ quite similar ~~indeed~~. Besides, at the end of stage 1 (section 3.1), T_s remains close to initial conditions, therefore ~~to~~ a ~~fixed~~ linear gradient of slope $\Delta T / H - G = -1/H$ is justified. Since the maximum temperature difference between the two phases is observed starting from the end of stage 1 and during stage 2 (section 3.2), it does not seem unreasonable to consider this hypothetical case for ~~retrieving~~deriving the maximum temperature difference. Using these assumptions, Eq. (18) ~~resumes~~ ~~to~~(20) becomes:

$$\frac{\partial^2(T_f - T_s)}{\partial x^2} - Pe \frac{\partial(T_f - T_s)}{\partial z} - (T_f - T_s) = -Pe G \quad (21)$$

Formatiert: Schriftfarbe: Rot

Formatiert: Schriftart: Kursiv

While in the general case of Eq. (20) the temperature difference implicitly depends on ϕ_0 , i.e. on the three non-dimensional parameters Pe , ϕ_0 , and G , Eq. (21) does no more depend on ϕ_0 because we replaced $\partial T_s(\phi_0)/\partial z$ by $-G$ which is independent

$$\text{of } \phi_0: \text{Eq. } \frac{1}{A} \frac{\partial^2 (T_f - T_s)}{\partial z^2} - \frac{Pe}{A} \frac{\partial (T_f - T_s)}{\partial z} - \frac{1}{1-\phi} (T_f - T_s) = -\frac{Pe \Delta T}{A H} \quad (19)$$

Eq. (19(21) is a second order ordinary differential equation for $(T_f - T_s)$ whose solution can be analytically retrieved and is given in Eq. (20) to (22) (details on the equation analytical solving are given in the derived as (see supplementary material) for details)

$$T_f - T_s = \alpha e^{r_1 z} + \beta e^{r_2 z} + (1-\phi) \frac{Pe \Delta T}{A H}, \quad (20-PeG) \quad (22)$$

where r_1 and r_2 are the roots of the associated equation of Eq. (19(21))

$$r_1 = \frac{Pe - \sqrt{Pe^2 + 4A}}{2}, \frac{1}{2} (Pe - \sqrt{Pe^2 + 4}), \quad r_2 = \frac{Pe + \sqrt{Pe^2 + 4A}}{2}, \quad (21 \frac{1}{2} (Pe + \sqrt{Pe^2 + 4})) \quad (23)$$

The parameters α and β are constrained by the boundary conditions for $(T_f - T_s)$ $((T_f - T_s) = 0$ at $z = 0$ and $\frac{\partial (T_f - T_s)}{\partial z} = 0$ at $z = H$)

$$\alpha = (1-\phi) \frac{Pe \Delta T}{A H} \frac{r_2}{r_2 e^{(r_1 - r_2)H} - r_1}, \quad \beta = (1-\phi) \frac{Pe \Delta T}{A H} \frac{r_1}{r_1 e^{(r_1 - r_2)H} - r_2}, \quad (22)$$

$$\text{and then } \alpha = PeG \frac{r_2}{r_1 e^{(r_1 - r_2)/G} - r_2}, \quad \beta = PeG \frac{r_1}{r_2 e^{(r_2 - r_1)/G} - r_1}. \quad (24)$$

The third term in Eq. (20(22)) is a particular solution for Eq. (19(21)).

4.2 Comparison with numerical models

From Eq. (20(22)) the maximum value of the depth-dependent temperature difference $(T_f - T_s)$ can be determined. It is found that the maximum is always at $z = H$. This value will be denoted as ΔT_{max} . Using this value the ratio of the analytical (Eq. 20) to the numerically determined ΔT_{max} and has been calculated for all 123 parameter combinations used for the numerical models studied and is shown as a function of Pe in Fig. S1 in the supplementary material. No correlation with Pe is observed. For 91% of the models, these ratios lie within 0.99 and 1.02, and all but one models analytical solutions are plotted as solid lines together with the numerical solutions (asterisks). The agreement is very good, for most cases the differences between 0.98 and the numerical and analytical solutions are well below 1%, only when ΔT_{max} reaches values of about 0.6 and higher the differences become $\geq 1.05\%$, up to 6%. This surprisingly general good agreement is another justification for using the time-independent equation (19(21)) to retrieve obtain an analytical solution of an intrinsically time-dependent process as long as we are interested only in the maximum value of $(T_f - T_s)$. Other reasons for the observed differences between the analytical and

Formatiert: Tabstopps: 7,36 cm, Links

Formatiert: Schriftfarbe: Rot

numerical solutions include numerical errors when determining the particular times when maximum temperature differences are reached, especially for the models which are in the regime close to $AT_{max} = 1$ where the $AT_{max}(Pe)$ – curves become non-linear (Fig. 3a) transient regime.

Formatiert: Schriftfarbe: Rot

4.3 Scaling laws for temperature differences at certain parameter limits

Formatiert: Schriftfarbe: Rot

The analytical solution for AT_{max} fits very well with our model results and therefore looks to be ideal for getting a better understanding on the relative influences of the ~~three~~two controlling parameters Pe and G , described in section 2.2 and 2.3. The Peclet number is already known to be of great importance for thermal equilibrium/non-equilibrium conditions. Although less commented for non-equilibrium build-up, the heat transfer number A controls local heat transfer between the two phases. We noticed in section 3.2 that there exist a high A and a low A regime with different non-equilibrium behavior. Inspecting the last term in Eq. (2022) we notice that a high Pe and a high initial thermal gradient should favor higher temperature differences, while a high A would rather favor thermal equilibrium. The porosity ϕ . This has been demonstrated in the form of $(1-\phi)$, also influences thermal equilibrium conditions, as expected in section 3.2: Fig. 3. Eq. (2022) is, however, complexcomplicated, and the visibility-on-assessment of the relative importance of these controlling parameters Pe and of the conditions G for different possible regimes is limited. In this section, we study the evolution of $(T_f - T_s)$, i.e. also AT_{max} , in a few limiting cases. This enables us to better understandunderstanding each parameter influence and to derive some scaling laws for different regimes.

4.3.1 Limit $A \rightarrow 0, Pe \rightarrow 0$

Formatiert: Englisch (Vereinigte Staaten)

Linearizing Eq. (20) with respectWhen Pe tends to A , around $A=0$, usingwe have the Taylor series in terms of A , we derive condition

Formatiert: Schriftfarbe: Rot

$Pe \ll 2$ (25)

With this condition Eq. (22) tends to the following limit for $(T_f - T_s)$ (see supplementary material for more details):

Formatiert: Tabstopps: Nicht an 1,88 cm

$T_f - T_s = PeG(1 - M)$ (26)

with

$M = \frac{\cosh(z) + \cosh(\frac{z}{G})}{1 + \cosh(2/G)}$ (27)

Formatiert: Tabstopps: 1,88 cm, Links

$T_f - T_s = \frac{AT}{H} \left(z + \frac{1}{PeGPeH} (1 - e^{PeGz}) \right)$ (23)

The limit for AT_{max} is simply obtained by setting $z = H$. The limit (23) can also be retrieved by neglecting the heat transfer term (left hand third term) in Eq. (19), which becomes negligible when A tends to 0, and solving the resulting equation. From Eq. (23) we notice that when A tends to 0 the temperature difference between the two phases does not depend on A anymore. It should be noted that this limit is valid only as long as Pe remains finite in the limit $A \rightarrow 0$. Further details of the comparison of Eq. (23) to the full analytical solution are discussed in the supplementary material.

365 **4.3.2 Limit $A \rightarrow \infty$**

When A tends towards infinity, which simplifies for $z = H = 1/G$ to

$$M = \frac{1}{\cosh(1/G)} \tag{28}$$

This is the limit for $Pe \rightarrow 0$. This limit ~~Eq. (20)~~ tends to the following limit:

$$T_f - T_s = (1 - \phi) \frac{Pe \Delta T}{A H} \tag{24}$$

370 Using this limit, we find values in very good agreement with those predicted by Eq. (20) for $A > 1$. See also Fig. S2b in the supplementary material.

4.3.3 Limit $Pe \rightarrow 0$

When Pe tends to 0, Eq. (20) tends to the following limit (see supplementary material):

$$T_f - T_s = (1 - \phi) \frac{Pe \Delta T}{A H} \left(1 - \frac{e^{-\frac{\sqrt{A}}{\sqrt{(1-\phi)} z}}}{1 + e^{-\frac{\sqrt{A}}{\sqrt{(1-\phi)} 2H}}} - \frac{e^{-\frac{\sqrt{A}}{\sqrt{(1-\phi)} z}}}{1 + e^{-\frac{\sqrt{A}}{\sqrt{(1-\phi)} 2H}}} \right) \tag{25}$$

375 This limit gives predictions for ΔT_{max} in very good agreement with Eq. (2022) for $Pe < 1$ (having $A=1$ and $\phi=0.1G = 0.1$) (see Fig. S2aS1 in the supplementary material).

If in addition A tends to zero, In the limit $G \rightarrow 0$ and finite $Pe < 1/G$ we get the following limit: for M

$$M \rightarrow e^{-z}$$

Thus, for both small Pe and small G the temperature difference (Eq. 26) can be written

380
$$T_f - T_s = PeG(1 - e^{-z}) \tag{29}$$

~~Eq.~~
$$T_f - T_s = Pe \Delta T z \left(1 - \frac{z}{2H} \right) \tag{26}$$

which is in agreement with the observation of a proportional relationship between Pe and ΔT_{max} for small A and small Pe (ΔT was non-dimensional and equal to 1 in all models). For more discussion, see supplementary material.

(29) confirms the proportionalities observed in Fig. 3, namely $\Delta T_{max} \propto Pe$ (Fig. 3a), and $\Delta T_{max} \propto G$ (Fig. 1b), respectively.

385 **4.3.42 Limit $Pe \rightarrow \infty$**

To obtain the limit of Eq. (2022) for $Pe \rightarrow \infty$, Eq. (2022) can be linearized with respect to $4A/((1-\phi)Pe^2) \ll 1.4/Pe^2 \ll 1$. Applying the rule of L'Hospital/Hôpital Eq. (2022) tends to the following limit (for arbitrary A):

$$T_f - T_s = \frac{\Delta T}{H} z - Gz \tag{27}$$

(30)

390 For details, see supplementary material. This limit is also the solution of Eq. (1921) when neglecting the diffusive and heat transfer terms. As demonstrated in the supplementary material this limit predicts ΔT_{max} values in very good agreement with Eq. (2022) for $Pe > 100$.

Formatiert: Tabstopps: Nicht an 1,88 cm
Formatiert: Schriftart: Kursiv

Formatiert: Schriftfarbe: Rot

Formatiert: Tabstopps: 1,88 cm, Links

4.3.5 Limit $\phi \rightarrow 1$

In Eq. (20), the presence of ϕ is always in the form of $A/(1-\phi)$. Therefore ϕ tending to 1 has the same limit as A tending towards infinity (Eq. 24). This limit approaches values predicted by Eq. (20) for high ϕ values (Fig.S2d in the supplementary material).

4.3.6 Exploring the domains for the maximum temperature difference including all limits

Before exploring the full parameter space we first give a short overview of expected parameter ranges in magmatic systems. In natural magmatic systems such as mid-ocean ridges, Pe is expected to evolve from very low values of order 10^{-5} to 10^{-3} in partially molten regions with distributed porous flow to higher values of order 1 or larger at depths where channels have merged, and further to very high values of order 10^5 in dyke systems (Schmeling et al., 2018). As A scales with the ratio of the channel width to the interfacial boundary layer thickness, A would evolve proportionally with the width of melt pathways which may increase by 3 to 5 orders of magnitude as 3D grain junctions eventually merge to 1D dykes. Additionally, as A is inversely proportional to the interfacial boundary layer thickness which increases with time, A should evolve with time, from high values at melt flow onset to much smaller values in highly evolved systems. In Figure 6 of Schmeling et al. (2018) the time-dependent interfacial heat flow has been determined which roughly maps into A if multiplied by $\frac{\phi}{(1-\phi)}$. This suggests A values dropping from about 10 to 10^{-5} over the time scale until thermal equilibrium is reached.

While the melt fraction does not influence ΔT_{max} (c.f. Eq. (22, 30)) it influences the long term temporal behavior once T_i is ϕ_0 - dependent (c.f. Eq. (20)). Therefore some words about possible melt fractions. As melt flow may occur at very small melt fractions (McKenzie, 2000; Landwehr et al., 2001), large ϕ - values are not expected in natural mantle magmatic systems, nor in dyke systems in the crust. Values of channel volume fraction generally remain below a few percent up to tens of percent (in dunite channels up to 10 - 20%, Kelemen et al., 1997). $(1-\phi)$ would therefore not vary over more than one order of magnitude, making the porosity a less influential parameter on thermal non-equilibrium build up in magmatic systems. Indeed, we explored the dependence of ΔT_{max} on ϕ , for a number of very different combinations of Pe and A values. Within possible ranges of Pe between 10^{-10} to 10^5 and A between 10^{-6} and 10^3 resulting variations of ΔT_{max} with mantle realistic ϕ values (0—20%) are only of about 0.01 if normalized by ΔT_{i_0} .

Because to get an idea about the expected order of this relatively small influence magnitude of ϕ on ΔT_{max} , the macroscopic dimension $G = 1/H$ of the system we here have to evaluate the scaling length L used to scale the dimensional H . L scales with the geometric mean of the channel width d_f and the interfacial boundary layer thickness δ (Eq. 9 with 11). L would evolve non-linearly with the width of melt pathways which may increase by several orders of magnitude as 3D grain junctions eventually merge to 1D dykes. As will be shown in section 5.3 in more detail the resulting non-dimensional G ranges between order 1 to order 10^{-5} .

In Figure 4 we explore ΔT_{max} variations using the analytical solution Eq. (2022), in which ΔT_{max} depends essentially on Pe and A , and the reference value for ϕ is chosen as 0.1. In the resulting Pe — A diagram three G . Three main regimes can be distinguished (Fig. 4):

Formatiert: Schriftfarbe: Text 1

Formatiert: Schriftfarbe: Text 1

Formatiert: Schriftfarbe: Rot

Formatiert: Schriftfarbe: Text 1

Formatiert: Schriftfarbe: Text 1

Formatiert: Schriftfarbe: Text 1

Formatiert: Schriftfarbe: Text 1

Formatiert: Schriftart: Kursiv

- Regime 1: For high Pe values, $(T_f - T_s)$ tends to the relationship described in Eq. (2730). The temperature difference increases linearly with distance from the bottom ($z = 0$) reaching $\Delta T_{max} = 1$ at $z = \frac{4H}{\epsilon}$. In the whole region the fluid temperature remains constant and at maximum 1 while the solid temperature increases linearly with z from 0 to 1.
- Regime 2: For small A values and $Pe \ll 1$ or more precisely, for $Pe \ll \frac{1}{G}$ represented by the oblique dashed line in Fig. 4, $(T_f - T_s)$ is also dependent on the varies with distance from the bottom; according to $(1 - e^{-z})$, and is proportional to Pe , while A and ϕ influences are negligible; and G . This means that large temperature gradients favor large temperature differences. In this domain, $(T_f - T_s)$ tends to the relationships presented in Eq. (25) and (26)-(29).
- Regime 3: For high A values and $Pe/A \ll 1$ large initial temperature gradient G close to 1 (small H) and $Pe \ll 1$, $(T_f - T_s)$ tends to the relationship proposed in Eq. (2426). In this domain, $(T_f - T_s) = \Delta T_{max}$ is proportional to Pe but no more dependent onto G . The depth, but is proportional to $(1 - \phi)$, Pe/A and to the initial solid temperature gradient; dependence is given by $(1 - M(z))$ which is identical to the solid temperature gradient at the top. However, numerical time dependent solutions show that $(T_f - T_s) = \Delta T_{max}$ is essentially independent of depth only during stage 1 and 2 (e.f. Section 3.1) and for sufficiently large H (> 5). Later it becomes depth-dependent and smaller than ΔT_{max} given by Eq. (24). $G = 1$ increases non-linearly from about 0 to 0.4 with increasing z .

Formatiert: Schriftart: Kursiv

Formatiert: Schriftart: 9 Pt., Kursiv, Englisch (Vereinigtes Königreich)

5 Discussion

5.1 Limitations

5.1.1 Comments on the analytic solution

Although the assumptions used to get the analytic solution (Eq. 2022) are very specific, they are reasonable considering the conditions in the models when ΔT_{max} is reached, and it fits very well the numerical results. This is shown in Fig. 5 where for various combinations of Pe , A , and HG the time-dependent temperature differences $(T_f - T_s)$ are shown as functions of depth together with the analytical solutions using Eq. (2022). For all examples the position of the maximum temperature differences lies at $z = H$. A major simplification used in Eq. (1921) was time-independence. Obviously, the resulting analytical solutions represent the stage 2, which is quasi steady state in contrast to stage 1 when the temperature difference builds up, and stage 3 when the long-term behavior is approached. We emphasize that this analytical solution is a very good approximation of the depth-dependent temporal maximum temperature difference that can be reached in such porous systems.

Formatiert: Schriftart: Kursiv

Formatiert: Schriftfarbe: Rot

5.1.2 Initial conditions and boundary conditions at top and initial conditions

The boundary conditions we chose at the top ($z = H$) are suitable for cases with little temperature evolution (regime 2), and 3, low Pe), and for early stages for regime 1 but might be inappropriate for high temperature increases (high Pe - regimes) - regime 1) at later stages (see section 4.3.64). In order to quantify the influence of this choice of boundary conditions on our

results, we compared the evolution of $(T_f - T_s)$ - profiles for three models, that belong to the three regimes identified in section 4.3.6 Peclet numbers and two heights H , using three different boundary conditions at the top: (Fig. 6):

- Constant heat flux/thermal gradient equal to the initial flux/thermal gradient in the solid and fluid phases (Neumann conditions/condition). This was the boundary condition used in the models.
- Heat flux/Thermal gradient is set to 0 at the top (Neumann conditions/condition).
- Both fluid and solid temperatures are set to 0 at the top (Dirichlet conditions/condition).
- Although top boundary conditions can strongly affect fluid temperature at the top is numerically calculated from the full equations (17) and solid temperature profiles (Fig. S 3, in supplementary material), their influence on $(T_f - T_s)$ is negligible (18) using one-sided (upwind) positions for regimes 1, the first and 3, except when getting close to the top of the domain. The choice of the second derivatives (open boundary).

Mathematically, the open boundary conditions has, however, condition is not a much stronger influence on the whole profile for regime 2, where rigorous boundary condition because both the temperature and temperature gradient intrinsically depend on the temperature evolution and within the model. Therefore, it cannot be applied to the analytical solution of section 4.1. Numerically it works well for our system without producing instabilities or oscillations. Comparing the top and bottom row of Fig. 6, the constant temperature gradient condition produces quite similar results as the open boundary condition for all Pe and H values tested during the first and second stage of temporal evolution (c.f. section 3.1). The agreement becomes worse for stage 3 when approaching steady state are controlled at large Pe . Comparing the other two boundary conditions (2nd and 3rd row of Fig. 6) with the constant gradient condition (top row) shows that the effect of the top boundary during stage 1 and 2 is still small sufficiently far away from the top. Only for the small Pe - case (left column of Fig. 6) the zero gradient and zero temperature conditions strongly affect the upper half of the domain by diffusion (see section 5.2 below), and are therefore very sensitive to. Yet the maximum temperature difference of the constant gradient case is nearly reached by the other two boundary conditions (see Fig. S3 further within the domain, not at the top. The special case of high Pe and high H with zero temperature boundary condition (3rd row 4th column in Fig. 6) shows a strong build-up of $T_f - T_s$ close to the top when approaching the steady state. This stems from the large local temperature gradient built up near the top as a result of transforming the difference in supplementary material). We summarize that advective heat in- and output ($Pe T_{influx} - Pe T_{outflux} = Pe$) into a high conductive outflux ($\partial T / \partial z$) at the top. It is unlikely that such situations occur in natural systems.

In summary, the influence of boundary conditions on fluid and solid temperatures evolution depends mostly on the domain size (H) and on the value of Pe . The larger these two parameters, the less important is the influence of boundary conditions within almost the whole model region/domain. If one is interested in the maximum value of $T_f - T_s$ in space and time, the tests show that this value can safely be picked at $z = H$ when using the constant temperature gradient boundary condition.

As an initial condition we used a linear temperature profile and initial equilibrium between solid and fluid. A non-linear initial temperature profile between $T_f = T_s = 1$ at the bottom and $T_f = T_s = 0$ at the top would have spatially varying temperature gradients with sections with gradients larger than those assumed in our model. As the temperature gradient strongly influences

Formatiert: Schriftart: Fett, Schriftfarbe: Rot

thermal non-equilibrium (see e.g. Eq. 2022 which explicitly contains the temperature gradient $\frac{\partial T}{\partial z}$), the above results are expected to be different, and a stronger thermal non-equilibrium is expected in regions with higher gradients. Schmeling et al. (2018) used a step function with $T_f = T_s = 1$ at $z = 0$ and $T_f = T_s = 0$ at $z > 0$ as initial condition, i.e. an extremely non-linear profile near $z = 0$. Assuming this initial temperature profile Figure 67 shows the temporal behavior of the temperature difference for selected parameter combinations, equal to the parameters used in Fig. 5. The analytical solutions for the time-independent case (Eq. 2022) is also shown. As expected, at early stages the temperature differences are significantly larger than given by the analytical solutions by a factor 2 or more shortly after the onset of the evolution. At later stages (stage 2 or 3) the time-dependent solutions approach or pass through the analytical solutions. Thus, we may state that the analytical solutions depicted in the regime diagram in Fig. 4 represent lower bounds of thermal non-equilibrium compared to settings with non-linear initial temperature profiles.

5.1.3 Densities Different densities and thermal properties of the two phases

While for simplicity we used equal physical properties for the fluid and solid, in many circumstances they might be significantly different. Equal properties are good approximations for magmatic systems where differences of density and thermal parameters are small (order of 10%), whereas porous flows of water or gases through rocks or other technical settings may be characterized by larger differences. Allowing for different material properties adds four new parameters, namely the ratio of diffusivities, the ratio of densities, the ratio of heat capacities and a new effective thermal conductivity λ_{eff} for the interface between the two phases with different properties. To evaluate how many new non-dimensional numbers are introduced we non-dimensionalize the equations assuming different material properties for the two phases. We use the fluid properties as scaling quantities and assume that they are independent of temperature, pressure and depth. Eq. (214) and (215) turn into: (for clarity, primes indicate non-dimensional quantities):

$$\frac{\partial T_f'}{\partial t'} + \frac{Pe}{A} \frac{1}{\lambda_{eff}'} v' \cdot \nabla T_f' = \frac{1}{\phi A \lambda_{eff}'} \phi \left(\frac{\partial T_f'}{\partial t'} + Pe v' \cdot \nabla T_f' \right) = \nabla \cdot (\phi \nabla T_f') - \frac{\phi_0}{\phi} (T_f' \phi_0 (1 - \phi_0) \lambda_{eff}') (T_f' - T_s') \quad (28(32))$$

and

$$\frac{\partial T_s'}{\partial t'} (1 - \phi) \frac{\partial T_s'}{\partial t'} = \frac{1}{(1 - \phi) A \lambda_{eff}'} \frac{\kappa_s'}{\rho_s' c_{p,s}'} \nabla \cdot ((1 - \phi) \nabla T_s') + \frac{\phi_0}{(1 - \phi) \rho_s' c_{p,s}'} \phi_0 (1 - \phi_0) \frac{\lambda_{eff}'}{\rho_s' c_{p,s}'} (T_f' - T_s') \quad (29(33))$$

Inspection of these equations shows that ~~two~~three more non-dimensional numbers are introduced: the ratio of diffusivities κ_s' , and the ratio of the products density and heat capacity, $\rho_s' c_{p,s}'$. The', and a new effective conductivity for heat transfer, λ_{eff}' . can be merged with A to define a new heat transfer number $A \lambda_{eff}'$.

As equations (2832) and (2933) cannot be merged into one time-independent ordinary differential equation for $(T_f - T_s)$ as in section 4.1, we numerically tested some cases with $Pe = 1$ and $A \lambda_{eff}' = 1$ in which the diffusivity ratios and the ratios of $\rho_s' c_{p,s}'$ were varied between 0.1 and 10 (see Fig. S4 in the supplementary material).8). The results show that for the fixed

Formatiert: Schriftfarbe: Rot

combination of $Pe = 1$ and $A\lambda'_{eff} = 1$ the magnitude of thermal non-equilibrium remains in the same order of magnitude
520 $O(0.1)$ as for equal properties (Fig. 5a). ~~However, the~~ 8). The time-dependence is significantly ~~effected~~ affected: For a high
ratio $\kappa'_s = 10$ (i.e. the solid is strongly conducting) the solid temperature profile remains close to the constant initial
gradient, and the temperature difference rapidly converges to a steady state similar to the analytical solution depicted in Fig. 5
~~a5a~~. In contrast, for a low $\kappa'_s = 0.1$ the solid temperature departs more strongly from the initial linear gradient, and the solid –
fluid temperature difference slowly drops with time on the long term. Varying the potential to store heat in the solid, i.e.
525 $\rho'_s c_{p,s}'$, Fig. 8e and f shows that a high value slows down the long term time-dependent variations, while a small value leads
to rapid long term temporal variations of $(T_f - T_s)$ and some differences in faster convergence to the final steady states (Fig.
54e and f in state which is similar to the supplementary material) equal properties case.

It is interesting to apply the results for different physical properties to a geologically relevant setting, namely water flowing
through sedimentary rocks. Given that the high heat capacity of water is about three times larger than that of rock, and the
530 density is almost three times less, the product $\rho'_s c_{p,s}'$ is about 0.78, i.e. of order 1. However, the thermal diffusivity of water
is significantly smaller than that of rock, typically by a factor 16, i.e. κ'_s is about 16. We tested a few cases (Fig. 9) with Peclet
numbers and A initial thermal gradients G (i.e. inverse model heights) (assuming for simplicity $\lambda'_{eff} = 1$) equal to the cases
depicted in Fig. 5. The time dependent profiles behave similarly to those in Fig. 5, with very similar maxima of the temperature
differences (red dashed curves in Fig. 5) relevant for stage 2. The only important difference is that the water-sedimentary rock
535 case more rapidly approaches the late steady states of stage 3 and these stages are closer to the maximum red-dashed curves.
~~The full set of results is shown in the supplementary material in Fig. S5.~~ These results suggest that the absolute values of
maximum thermal non-equilibrium temperature differences shown in the regime diagram Fig. 4 are also applicable to a water-
sedimentary rock system.

5.1.4 Heat transfer number A

540 As is evident from our scaling, the interfacial heat transfer Q_B scales with the heat transfer number A , i.e. $Q_B \propto A$. In the
previous sections A was chosen constant. In reality A is expected to change with time as the microscopic boundary layers
thicken with time. Schmeling et al. (2018) explicitly solved for the time dependent variation of the interfacial heat transfer by
applying a convolution integration over the past history of the thermal evolution. As this is numerically expensive, a first order
step in this direction is to consider a spatially constant but time-dependent A using boundary layer theory. To test this idea we
545 replace the parameter A used in the non-dimensionalization (Eq. 9) by a constant A_0 and use a microscopic thermal boundary
layer thickening proportional to the square root of time, $dm = c_{th} \sqrt{\kappa_0 t}$, where c_{th} is a constant of order 2.32 for a cooling
half-space (Tureotte and Schubert, 2014). Applying our non-dimensionalization a time-dependent A can be defined as

$$A = \frac{c_{\sqrt{A_0}}}{c_{th} \sqrt{\kappa_0 t}} \quad (30)$$

Formatiert: Schriftfarbe: Rot

From Eq. (30) it is clear that at the onset of our experiments A is very large and then drops as time proceeds. Thus, from the regime diagram (Fig. 4) it is expected that in the early stage a large A will lead to small temperature differences, while during later stages A decreases, i.e. heat transfer between solid and fluid decreases, and thermal non-equilibrium might be built up. To include a varying $A(t')$ according to Eq. (30) the non-dimensional heat equations for the fluid and solid, Eq. (12) and (13), respectively, are modified by replacing all occurrences of A by A_0 and multiplying the heat exchange terms (last terms) in both equations with $A(t')/A_0$. We carried out a few tests for similar parameters as chosen in Fig. 5, namely $Pe = 0.01, 1, 100$, $A_0 = 0.01, 1, 100$. The results are shown in Fig. S6 in the supplementary material. It should be noted that from Eq. (30) a small $A_0 = 0.01$ corresponds to a time-dependent $A(t')$ dropping from order 1 to 0.01, and a large $A_0 = 100$ corresponds to a time-dependent $A(t')$ dropping from order 100 to 1 during the time period of interest. Comparing the time-dependent A -models with the constant A -models shows: 1) the temporal behavior of $(T_f - T_s)$ is stronger for the variable A models, and 2) the late stages are characterized by significantly larger $(T_f - T_s)$ differences than the analytical maximum curves (dashed red) in Fig. 5. Only models with small A_0 and large Pe remain comparable to models with constant A_0 . Thus, we may state here that the thermal non-equilibrium temperature differences given in the regime diagram (Fig. 4) provide lower bounds for systems in which the heat transfer parameter is allowed to vary with time. Qualitatively, a time-dependent A shifts the boundary between large and small temperature differences in the regime diagram to the right and downwards. More work needs to be done to fully explore the regime diagram for time-dependent A and compare such models with the fully consistent solutions of Schmeling et al. (2018).

5.1.5 Spatially constant parameters

Here we assumed spatially constant parameters ϕ, Pe, A . In reality, percolating melt may focus into channels which subsequently merge forming anastomosing systems (Spiegelman et al., 2001; Hart, 1993). If such systems are still described by effective macroscopic properties, these parameters change with depth. For such depth-dependent parameters the regime diagram (Fig. 4) still is useful to provide first order estimates of thermal non-equilibrium temperature differences by identifying the regimes in which the parameters are expected to vary with depth. A more rigorous evaluation of thermal non-equilibrium temperatures for well-defined anastomosing systems with prescribed parameters $\phi(z), Pe(z), A(z)$ will be presented in another paper (Chevalier and Schmeling, in prep.).

5.2 Time scales

It is interesting to evaluate the time scales for reaching the maximum non-equilibrium temperature differences and the steady state. For every [numerical](#) model, we recorded the time needed to reach 90% of the maximum temperature differences between fluid and solid, $t_{90\%}$, and the time needed to reach steady-state, t_{steady} . [The latter has been determined as the time at which the maximum difference between \$\(T_f\(z\) - T_s\(z\)\)\$ – curves at two subsequent time steps becomes less than \$10^{-8} \Delta T_{max}\$.](#) These times can be compared with different time scales that may characterize the evolution of temperatures in the models. These

time scales can be based on advection over a characteristic distance d_{char} and reading $t_{adv} = d_{char}/v_0$, or on diffusion over the characteristic distance giving $t_{diff} = d_{char}^2/(\epsilon_{th}^2 \kappa_0)$. We tested these time scales with various the two natural length scales of the models, namely, the prescribed boundary layer thickness, dm . The first is the scaling length L (= 1 non-dimensional) representing essentially the geometric mean $\sqrt{(dmL_0)}$ which corresponds to the scaling time t_0 of the channel width L_0 of the pores, d_f , and the interfacial boundary layer thickness δ . The second is the model height H . Grouping the models depending on the regime they belong to (see section 4.3.4, and Fig. 4), we plotted the recorded times $t_{90\%}$ and t_{steady} versus the characteristic time scales mentioned above. Good agreement with the characteristic time scales is indicated by observed times fitting to the dashed $x = y$ - lines (Figure 10). Grouping the models depending on the regime (see section 4.3.6, and Fig. 4) they belong to, we plotted the recorded times $t_{90\%}$ and the time to reach steady state versus the characteristic time scales mentioned above to evaluate which time scale fits best to the observed times. The result is shown in Figure 7.

- In regime 1 (high Pe), $t_{90\%}$ is proportional to t_{advH} (Figure 7a, 10a, blue circles). In this regime the high value of $-Pe$ makes the fluid temperature increase fast. It reaches its maximum value during the time under which significant fluid-solid heat transfer occurs, after builds up and the solid temperature is still low. This corresponds to the time for traveling the full distance H . Depending on During stage 2 and 3 the value of A , which quantifies the efficiency of heat transfer, solid temperature increases and the temperature difference can then decrease decreases before steady state is reached. The time for reaching steady state (Fig. 7b 10b, circles) varies almost roughly linearly with $t_{steady} \propto t_{diffH}$ but is up to one orders of magnitude larger. Clearly it is also controlled by diffusion. In this regime fluid temperature increases rapidly, then solid temperature increases, possibly leading to further fluid temperature increase, until heat transfer and diffusion equilibrate for the solid that reaches a steady state t_{diffH} . For most cases it is controlled by diffusion through the solid over distances of order H . The case with large H (circle in Fig. 10b below dashed line) apparently reaches the steady state earlier, but still later than on a corresponding advective time scale based on H (not shown). Inspecting this model shows that during stage 2 and 3 the high Pe number facilitates approaching thermal equilibrium rapidly within large parts of the model and reducing the effective length scale (and characteristic timescale) over which still non-equilibrium is present.
- In regime 2 (low Pe and low $AG < 0.1$, i.e. $H > 10$) the time for reaching ΔT_{max} is controlled by interfacial heat transfer (Fig. 7a, 10a, red asterisks) on the length scale $\sqrt{(dmL_0)}$ as long as L resulting in $t_{90\%}$ is proportional to t_0 , but for very small A (higher t_0 , equivalent to inefficient heat transfer) thermal non-equilibrium is reached earlier than t_0 as it is limited by diffusion through the whole domain which is probably the reason for flattening the $t_{90\%}$ curve. The time for reaching steady state is controlled by the diffusion time scale across the height of the system (Fig. 7b), but after a somewhat longer time, 10b).

- In regime 3, (low $Pe/A \ll 1$, $A \gg 1$), and high G (small H), time for reaching ΔT_{max} depends mostly on A (i.e. interfacial is similar or shorter than the diffusion on the length scale $\sqrt{(d_m L_0)}$). In this regime, heat transfer is no more negligible compared with advection, and limits time based on the temperature difference model height H (Fig. 10a, black crosses). The flattening of the curve indicates that can develop. Steady state non-equilibrium is reached at a time that faster for some models because Pe reaches order 1 and the advective timescale starts to take over. The time for reaching steady state (Fig. 10b, crosses) varies linearly with $t_{steady} \propto t_{diffH}$. Clearly, it is also controlled by advection time scale (not shown), but limited by diffusion time scale (Fig. 7b, crosses).

5.3 Applications to magmatic systems

We now test the possible occurrence of thermal non-equilibrium in natural magmatic systems based on the suggested controlling non-dimensional parameters, namely the Peclet number Pe , the initial thermal gradient $G (= 1/H)$, and the heat transfer number A . Due to the smaller importance of melt fraction ϕ (cf. section 4.3.6) we neglect the influence of ϕ and focus on Pe and A only. Typical stages of melt flow stages for mid-ocean ridges include stage a), partially molten regions with interstitial melts sitting at grain corners, grain edges or grain faces with low (0.0001 - 6%) melt fractions (see e.g. the discussion in Schmeling, 2006), stage b), merging melt channel or vein systems with high (> 10 - 20%) porosity channels identified as dunite channels after complete melt extraction (Kelemen et al., 1997), and stage c), propagating dykes or other volcanic conduits. Let's assume typical overall melt fractions of 1% to 20% for stages b) and c). Schmeling et al. (2018) discussed possible Peclet numbers for such systems based on a Darcy flow based related Peclet number

$$Pe_D = \frac{v_D d_s}{\kappa_0} \quad (34)$$

which relates to A s we preferably use the melt pore dimension d_f in our scalings (Eq. 9a and 10a) we need to relate it to the solid phase dimension d_s by using

$$d_s = d_f \frac{g}{\phi} = \begin{cases} (1 - \phi) & \text{melt channels} \\ \sqrt{\phi}(1 - \sqrt{\phi}) & \text{melt tubes} \end{cases} \quad (35)$$

Using (35), (9a), and (16) we arrive at the Peclet number used here by

$$Pe = Pe_D / (1 - \phi) \text{ for melt in channels or } Pe = Pe_D / (\sqrt{\phi}(1 - \sqrt{\phi})) \text{ for melt in tubes. } Pe_D \frac{1}{g \sqrt{c}} \sqrt{\frac{(1 - \phi) \delta}{d_f}} \quad (36)$$

Schmeling et al. (2018) reviewed and estimated typical pore or channel spacings d_c of $10^{-3} - 10^{-2}$ m for stage a), 0.1 m for early stage b) increasing to 1 - 100 m for late stage b), and 100m - 300 m for stage c) (dykes). Arguing for typical geometries, spreading rates and melt extraction rates Schmeling et al. 2018 estimated the Darcy velocity lying between 10^{-10} m/s and 10^{-9} m/s. With these parameteres Pe_D - numbers for the three stages can be estimated as 10^{-8} to 10^{-7} to 10^{-5} for stage a), 10^{-5} to 10^{-4} to 10^{-3} for stage b) at depths where channel distances are of order 0.1 m, and 10^{-4} to 0.1 at shallower depths where the channel

Formatiert: Schriftfarbe: Text 1

distances have increased to the order of 1 m to 10^3 m, and $>10^4$ for the dyke stage c). Obviously, the Peclet number used here is of the same order as Pe_D for melt in tabular channels, but may be about one half order of magnitude larger than Pe_D for tubular melt conduits.

To estimate realistic ranges for A Peclet numbers as defined here (Eq. 36) typical interfacial thermal boundary layer thicknesses may be considered for the above mentioned stages. Following δ are needed. As the arguments from section 5.1.4 thermal interfacial heat exchange intrinsically is time-dependent a good estimate for the interfacial boundary layer thickness is $\delta = c_{th} \sqrt{\kappa_0 t}$ (in dimensional form) where c_{th} is a constant for a thermal boundary layer, equal to 2.32 for a cooling half space. Assuming that the characteristic time can be expressed by the (dimensional) fluid velocity v_0 and system height H , i.e. by $t = H/v_0 = H\phi/v_D$, we may express δ in terms of the Peclet number Pe_D . With the resulting t and subsequent δ we obtain a scaling law for A : δ we arrive at the following Peclet number (H and d_f are dimensional or non-dimensional):

$$A = \sqrt{Pe} \sqrt{\frac{L_0}{H}} \quad (32)$$

$$Pe = Pe_D^{3/4} \sqrt{\frac{c_{th}}{c}} g^{-3/4} \left(\frac{H}{d_f}\right)^{1/4} \sqrt{1-\phi} \quad (37)$$

For mid ocean ridge settings we assume H of the order 1 to 10 km, and L_0 use Eq. (35) to insert typical d_f -values (increasing from 10^{-4} m (stage a), interstitial melts) to 10^{-3} m to 10^{-1} m for the channeling stage b) (see Schmeling et al., 2018) to >10 m for the dyke stage c). With these estimates the above scaling law The resulting Peclet number (Eq. 32) allows estimating A (37) is of the order 10^{-3} to $10^{-0.5}$ for stage a), order 10^{-5} to 10^{-2} during the early phase stage b) and order $10^{-4.5}$ to $10^{-0.5}$ in 1 during the later phase stage b) appropriate for dunite systems for stage b), and order 10^{-4} to 10^7 for the dyke stage c). To estimate typical non-dimensional thermal gradients G' (or layer thickness H') the above estimate for δ and d_f can be inserted into the scaling length L (Eq. 9a) to arrive at a non-dimensional $G' = 1/H'$.

$$G' = \left(\frac{H}{d_f}\right)^{-3/4} g^{-1/2} \phi^{3/4} \sqrt{\frac{c_{th}}{c}} Pe_D^{-1/4} \sqrt{1-\phi} \quad (38)$$

With the derived estimates for the three stages, G' is of the order 10^{-6} to $10^{-2.7}$ for stage a), 10^{-4} to $10^{-2.5}$ increasing to 10^{-4} - 0.6 for stage 2), and 10^{-5} to 10^{-2} for the dyke stage c). These resulting stages for Pe and AG' are indicated in Figure 4, the regime diagram (Fig. 4). Starting from interstitial melts at full thermal equilibrium, channeling and veining may result in moderate thermal non-equilibrium at sufficiently high thermal gradients, while after transition to dyking full thermal non-equilibrium is predicted.

A similar exercise could be made for continental magmatic systems. We skip such an explicit evaluation here but note that silicic melt viscosities are typically higher than those of basaltic melts at mid-ocean ridges. Thus, Peclet numbers and heat transfer numbers are expected to be smaller, but non-dimensional thermal gradients (Eq. 38) might be larger, resulting in a downward and leftward/rightward shift of the natural stages indicated in Figure 4.

To make our scaling laws and time scales for reaching maximum thermal non-equilibrium more accessible it is worth writing them in dimensional form. First, to estimate the Peclet number of a natural system combining Eq. (9) and (16) gives

Formatiert: Schriftart: Kursiv

Formatiert: Schriftfarbe: Rot

$$Pe = \frac{v_{f0}}{\kappa_0} \sqrt{\frac{\phi_0(1-\phi_0)\delta}{S}} \quad (39)$$

indicating that for very small or very large melt fractions Pe becomes very small. One may use Eq. (11) or (12) to write Pe also in terms of pore or grain dimensions d_f or d_s , respectively. The scaling laws and characteristic time scales for the three regimes we found (Fig. 4) are in dimensional form:

- Regime 1: For large Pe the maximum non-equilibrium temperature difference is simply equal to the imposed temperature difference, $\Delta T_{max} = \Delta T_0$, and the characteristic time to reach maximum non-equilibrium is simply $t_{char} = H/v_{f0}$, i.e. the total time of a fluid particle for passing through the system.

- Regime 2 and 3: For small Peclet number ($Pe < \frac{H\sqrt{S}}{\sqrt{\phi_0(1-\phi_0)\delta}}$) the maximum temperature difference scales like

$$\Delta T_{max} = \frac{G v_{f0} \phi_0 (1-\phi_0) \delta}{\kappa_0 S} \quad (40)$$

and the characteristic time for reaching this non-equilibrium scales with t_0 , i.e.

$$t_{char} = \frac{\phi_0 (1-\phi_0) \delta}{\kappa_0 S} \quad (41)$$

These relations can easily be used to assess the potential of thermal non-equilibrium in systems of fluid flow through solids with given geometrical properties and fluid fractions.

6 Conclusions

In conclusion we showed that in magmatic systems characterized by two-phase flows of melts with respect to solid, thermal non-equilibrium between melt and solid may arise and become important under certain conditions. The main conclusions are summarized as follows:

From non-dimensionalization of the governing equations three non-dimensional numbers can be identified controlling thermal non-equilibrium: the Peclet number Pe , the heat transfer number A , and the melt porosity ϕ , and the initial non-dimensional temperature gradient G in the system. The maximum possible non-equilibrium solid – fluid temperature difference ΔT_{max} is controlled only by two non-dimensional numbers: Pe and G . Both numerical and analytical solutions show that in a $Pe - AG$ - parameter space three regimes can be identified:

- In regime 1 (high Pe ($>1/G$)) strong thermal non-equilibrium develops independently of Pe and A , a non-dimensional scaling law $T_f - T_s = \frac{\Delta T}{H} G z$ has been derived.
- In regime 2 (low Pe ($<1/G$) and low A ($<1/G$ (<0.3))) non-equilibrium decreases proportionally to decreasing Pe and G , and the non-dimensional scaling law reads $T_f - T_s = Pe \Delta T z \left(1 - \frac{z}{2H}\right) Pe G (1 - e^{-z})$.
- In regime 3 (low Pe (<1) and large A ($\rightarrow G$ of order 1)) non-equilibrium scales with Pe/A and thus becomes unimportant G and is depth-dependent, the scaling law is $T_f - T_s = (1-\phi) \frac{Pe \Delta T}{A} Pe G (1 - M(z))$ where $M(z)$ depends on G .

Formatiert: Links

Formatiert: Schriftart: Kursiv

Formatiert: Schriftart: Kursiv

Further conclusions include:

- ~~The melt porosity ϕ has only a minor effect on thermal non-equilibrium.~~
- The time scales for reaching thermal non-equilibrium scale with the advective time-scale in the high Pe -regime and with the interfacial diffusion time in the other two low Pe number regimes.
- Applying the results to natural magmatic systems such as mid-ocean ridges can be done by estimating appropriate orders of Pe and AG . Plotting such typical ranges in the Pe - AG regime diagram reveals that a) interstitial melt flow is in thermal equilibrium, b) melt channeling as e.g. revealed by dunite channels may reach moderate thermal non-equilibrium, and c) the dyke regime is at full thermal non-equilibrium.
- In the studied setup G was constant leading to conservative estimates of thermal non-equilibrium. Any other depth-dependent initial temperature distributions generate higher non-equilibrium than reported here.
- The derived scaling laws for thermal non-equilibrium are valid for equal solid and fluid properties. Assuming different properties such as for a water – sandstone system results in similar maximum non-equilibrium temperature differences, but in significantly different time evolutions.

While for simplicity the presented approach has been done essentially for constant model parameters, it can easily be extended to vertically varying parameters. Thus, tools are provided for evaluating the transition from thermal equilibrium to non-equilibrium for anastomosing systems (Hart, 1993; Chevalier and Schmeling, in prep.).

7 Acknowledgements

We gratefully acknowledge the excellent reviews by John Rudge and Cian Wilson, who stimulated us into significantly improving the scaling. We acknowledge funding support by the Deutsche Forschungsgemeinschaft (DFG) with the grant no. 403710316.

References

- Aharonov, E., Whitehead, J.A., Kelemen, P. B., and Spiegelman, M.: Channeling instability of upwelling melt in the mantle. J. Geophys. Res., 100, 20,433 – 20,450, 1995.
- Amiri, A. and Vafai, K.: Analysis of Dispersion Effects and Non-Thermal Equilibrium, Non-Darcian, Variable Porosity Incompressible Flow Through Porous Media, Int. J. Heat Mass Transf., 37, 939-954, 1994.
- Becker, K. and Davis, E.: On situ determinations of the permeability of the igneous oceanic crust, in: Hydrogeology of the Oceanic Lithosphere, pp. 311–336, eds. Davis, E. & Elderfield, H., Cambridge Univ. Press, 2004.
- Bruce, P. M. and Huppert, H. E.: Solidification and melting along dykes by the laminar flow of basaltic magma. In Ryan, M. P., ed., Magma transport and storage. Chichester: Wiley, pp. 87-101, 1990.

Formatiert: Schriftfarbe: Rot

730 Davis, E.E. et al.: Regional heat flow variations across the sedimented Juan de Fuca ridge eastern flank: constraints on
 lithospheric cooling and lateral hydrothermal heat transport, *J. geophys. Res.*, 104, 17 675–17 688, 1999.
 de Lemos, M. J. S.: Thermal non-equilibrium in heterogeneous media, Springer Science+Business Media, Inc., 2016.
 Furbish, D. J.: Fluid Physics in geology. Oxford University Press, New York. 476 pp., 1997.
 Harris, R.N. and Chapman, D.S.: Deep seated oceanic heat flow, heat deficits and hydrothermal circulation, in *Hydrogeology*
 735 *of the Oceanic Lithosphere*, pp. 311–336, eds Davis, E. & Elderfield, H., Cambridge Univ. Press, 2004.
 Hart, S.R.: Equilibration during mantle melting: a fractal tree model. *Proc. Natl. Acad. Sci. USA* 90, 11,914–11,918, 1993.
 Kelemen, P. B., Whitehead, J. A., Aharonov, E., and Jordahl, K. A.: Experiments on flow focusing in soluble porous media,
 with applications to melt extraction from the mantle, *J. Geophys. Res.* 100, 475 – 496. doi.org/10.1029/94JB02544, 1995.
 Kelemen, P. B., Hirth, G., Shimizu, N., Spiegelman, M., and Dick, H. J. B.: A review of melt migration processes in the
 740 adiabatically upwelling mantle beneath oceanic spreading ridges. *Phil. Trans. R. Soc. Lond. A*, 355, 283 – 318, 1997.
 Keller, T., May, D. A., and Kaus, B. J. P.: Numerical modelling of magma dynamics coupled to tectonic deformation of
 lithosphere and crust, *Geophys. J. Int.*, 195.3, 1406-1442, 2013.
 Kuznetsov, A. V.: An investigation of a wave of temperature difference between solid and fluid phases in a porous packed
 bed, *Int. J. Heat Mass Transfer*, 37, 3030 – 3933, doi.org/10.1016/0017-9310(94)90358-1, 1994.
 745 Landwehr, D., Blundy, J., Chamorro-Perez, E. M., Hill, E., and Wood, B.: U-series disequilibria generated by partial melting
 of spinel lherzolite, *Earth Planet. Sci. Lett.*, 188 329-348, 2001.
 Lister, J. R. and Kerr, R. C.: Fluid-mechanical models of crack propagation and their application to magma transport in dykes.
J. Geophys. Res. 96, 10 049 – 10 077, 1991.
 Maccaferri, F., Bonafede, M., Rivalta, E.: A quantitative study of the mechanisms governing dike propagation, dike arrest and
 750 sill formation. *J. Volc. Geoth. Res.* 208, 39–50, 2011.
 McKenzie, D.: The generation and compaction of partially molten rock. *J. Petr.*, 25, 713-765, 1984.
 McKenzie, D.: Constraints on melt generation and transport from U-series activity ratios. *Chem. Geol.*, 162, 81 – 94, 2000.
 Minkowycz, W. J., Haji-Sheikh, A., Vafai, K.: On departure from local thermal equilibrium in porous media due to a rapidly
 changing heat source: the Sparrow number, *Int. J. Heat Mass Transf.*, 42 (18), 3373-3385, 1999.
 755 Nield, D. A. and Bejan, A.: *Convection in Porous Media*, Third Edition, Springer Science+Business Media, Inc., 2006.
 Rivalta, E., Taisne, B., Buger, A. P., and Katz, R. F.: A review of mechanical models of dike propagation: Schools of thought,
 results and future directions, *Tectonophysics*, 638, 1 – 42, 2015.
 Roy, M.: Thermal disequilibrium during melt-transport: Implications for the evolution of the lithosphere-asthenosphere
 boundary. arXiv preprint arXiv:2009.01496, 2020.
 760 Rubin, A. M.: Propagation of magma-filled cracks. *Annual Review of Earth and Planetary Sciences* 23, 287–336, 1995.
 Schmeling, H.: A model of episodic melt extraction for plumes, *J. Geophys. Res.*, 111, B03202, doi:10.1029/2004JB003423,
 2006.

Schmeling, H, Marquart, G, and Grebe, M.: A porous flow approach to model thermal non-equilibrium applicable to melt migration, *Geophys. J. Int.*, 212, 119-138, 2018.

765 Spiegelmann, M., Kelemen, P. B., Aharonov, E.: Causes and consequences of flow organization during melt transport: The reaction infiltration instability in compactible media. *J. Geophys. Res.*, 106, 2061 – 2077, 2001.

Spiga, G. and Spiga, M.: A rigorous solution to a heat transfer two phase model in porous media and packed beds, *Int. J. Heat Mass Transfer*, 24, 355 - 364, doi.org/10.1016/0017-9310(81)90043-0, 1981.

Turcotte, D. and Schubert, G.: *Geodynamics*. Cambridge University Press,Cambridge, 2014.

770 Verruijt, A.: *Theory of Groundwater Flow*. The Macmillan Press Ltd., London and Basingstoke. 141 pp. DOI 10.1007/978-1-349-16769-2, 1982.

Wilcock, W. S. D. and Fisher, A. T.: Geophysical constraints on the subseafloor environment near Mid-Ocean ridges, pp. 51 – 74, in: *Subseafloor Biosphere* , eds. C. Cary, E. Delong, D. Kelley, and W. S. D. Wilcock. Washington DC. American Geophysical Union, 2004.

775 Woods, A. W.: *Flow in Porous Rocks: Energy and Environmental Applications*. Cambridge University Press, Cambridge, 289 pp., 2015.

780

785

| Symbol | Definition | Units |
|--------------|--|-------|
| A | Heat transfer number, Eq. (10a,b) | - |

| | | |
|---------------------------------------|---|--------------------------------|
| $c_{p,f,s,0}$ | Specific heat at constant pressure for the fluid, solid, or reference, $\text{J kg}^{-1}\text{K}^{-1}$ respectively | |
| c, c_s | Geometrical constant, 2 for <u>fluid pore space or solid phase, respectively</u> . - <u>For melt channels, 4 or low porosity films $c = 2$, for tubes $c = 4$ (Eq. 9b, 10b, 11, 12)</u> | |
| c_{th} | Constant for thermal boundary layer, 2.32 for cooling half space | - |
| d_m | Interfacial boundary layer thickness | m |
| d_s, d_f | Characteristic length scale of solid or fluid phase, respectively | m |
| f | Subscript used for fluid | - |
| g | <u>Function describing part of the ϕ-dependence of d_f, d_s (Eq. 35)</u> | - |
| G | <u>Initial temperature gradient, taken positive for temperature decreasing with height</u> | K m^{-1} |
| H | Height of the model | m |
| L_0, L_Δ | Scaling length used for non-dimensionalization (d_f) (Eq. 9) | m |
| $M(z)$ | <u>Function describing the depth-dependence of analytical solution of $(T_f - T_s)$ for small Pe (Eq. 27)</u> | - |
| Pe, Pe_D | Peclet number, based on fluid velocity (Eq. (14) (16)) or based on Darcy velocity (Eq. 34), respectively | - |
| Q_{fs} | Interfacial heat exchange rate from fluid to solid | $\text{J s}^{-1}\text{m}^{-3}$ |
| r_1, r_2 | <u>Constants of analytical solution (Eq.. 23)</u> | - |

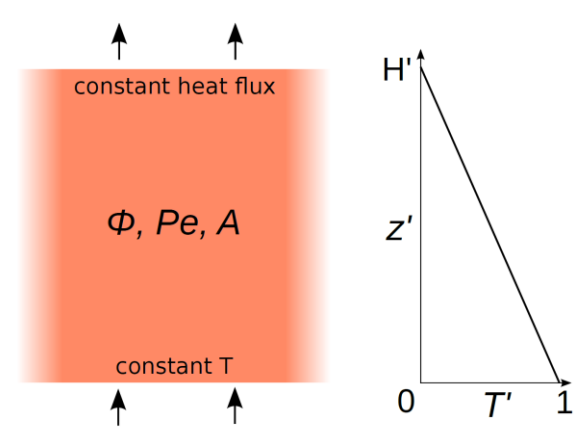
Formatiert: Schriftart: Kursiv

| | | |
|------------------------------|---|---------------------------------|
| s | Subscript used for solid | - |
| S | Interfacial area density, i.e. interfacial area per volume | m^{-1} |
| t, t_{char} | Time Time, characteristic timescales, respectively. “char” indicates the characteristic time for diffusion or advection over a characteristic length L or H : “diff L ”, “diff H ”, “adv L ”, “adv H ” | s |
| t_0 | Diffusion time on interfacial scale used for non-dimensionalization Scaling time (Eq. 10) | s |
| $T_{f,s}$ | Temperature of the fluid or solid, respectively | K |
| $\Delta T_0, \Delta T_{max}$ | Initial temperature difference between top and bottom used as scaling temperature, and maximum difference between fluid and solid temperature in space and time, respectively | K |
| $v_{f,s}$ | Velocity of the fluid or solid, respectively | m s^{-1} |
| $\bar{v}_g v_{f0}$ | Constant fluid velocity in the model, <u>used for scaling</u> | m s^{-1} |
| v_D | Volumetric Volumetric flow rate (Darcy velocity) ($= \phi \bar{v}_g v_f$) | m s^{-1} |
| x, y, z | Coordinates, distance | m |
| α, β | <u>Functions used for analytical solution (Eq. 24)</u> | - |
| δ | <u>Interfacial boundary layer thickness</u> | <u>m</u> |
| $\kappa_{f,s,0}$ | Thermal diffusivity of the fluid, solid or reference, respectively | $\text{m}^2 \text{s}^{-1}$ |
| $\lambda_{f,s}$ | Thermal conductivity of the fluid or solid, respectively | $\text{W m}^{-1} \text{K}^{-1}$ |
| λ_{eff} | Effective thermal conductivity at the solid-fluid interface | $\text{W m}^{-1} \text{K}^{-1}$ |

| | | |
|----------------|---|--------------------|
| ϕ, ϕ_0 | Porosity or scaling porosity, respectively | - |
| $\rho_{f,s,0}$ | Density of the fluid, solid, or reference. respectively | kg m^{-3} |

790

Table 1: Symbols, their definition, and physical units used in this study.



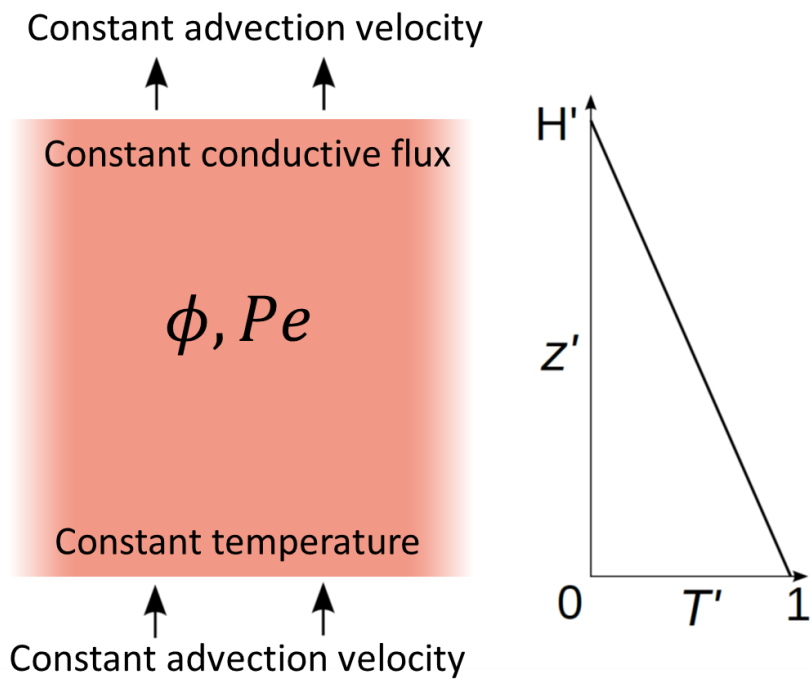
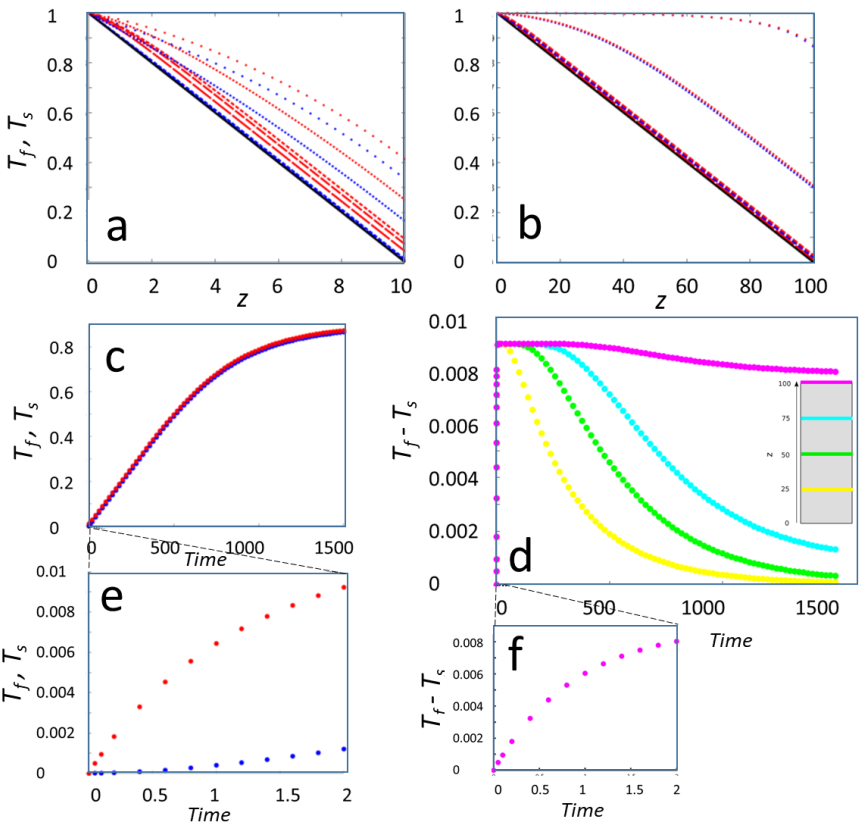


Figure 1. Initial and boundary conditions.



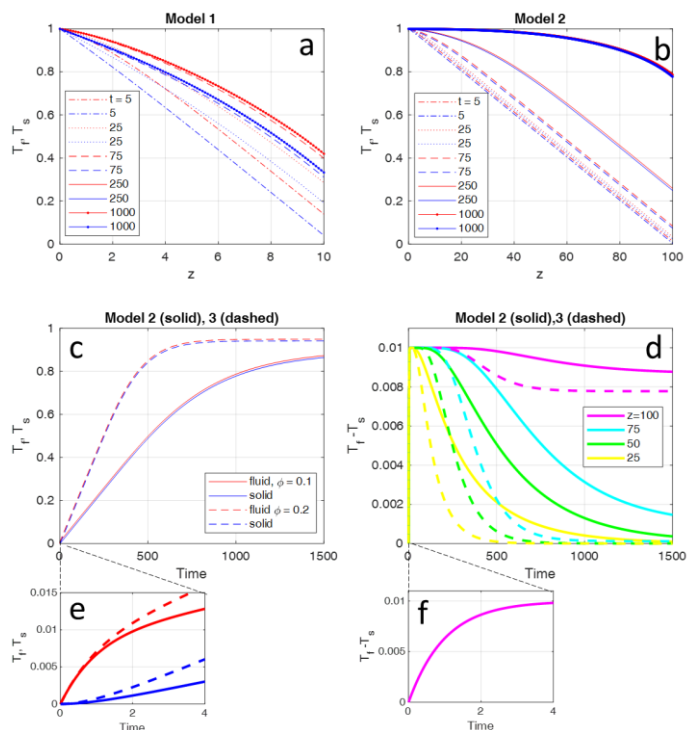
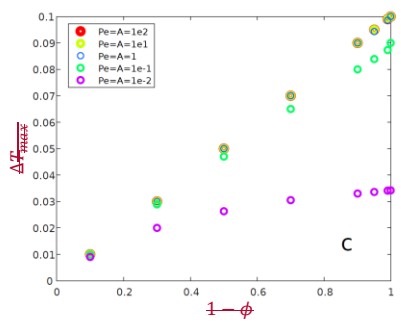
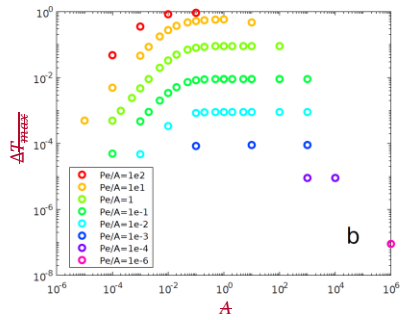
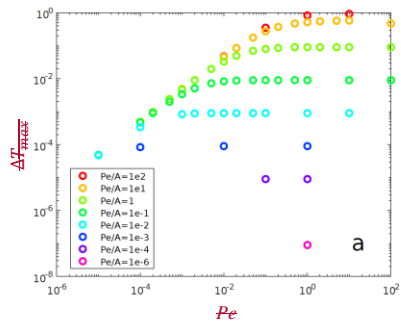


Figure 2. Typical model evolution for $Pe = 1$, $A = 1$, two different melt fractions $\phi = 0.1$, and two different heights H . a) Model 1 is with non-dimensional height $H = 10$, and $\phi = 0.1$. Red and blue curves show the fluid and solid temperatures at different times non-dimensional times t as indicated by the legend, respectively. Initial temperatures are in black, almost identical to the $t = 0.5$ curves. b) Model 2 with $H = 100$, else as in a). c) Temporal evolution of fluid and solid temperatures, T_f (red) and T_s (blue), respectively, of model 2 at the top of model 2 with $\phi = 0.1$ and model 3 with $\phi = 0.2$, $H = 100$ for both models. d) Evolution of fluid - solid temperature difference ($T_f - T_s$) at different distances z in model 2. The positions $z = 25, 50, 75, \text{ and } 100$ are indicated by the inset, ($\phi = 0.1$, solid curves) and in model 3 ($\phi = 0.2$, dashed curves). e) Zoomed-in early temporal evolution solid and fluid temperatures of model models 2 and 3 shown in c). f) Zoomed-in early temporal evolution of temperature difference of model 2 and 3 shown in d).

Formatiert: Schriftfarbe: Rot



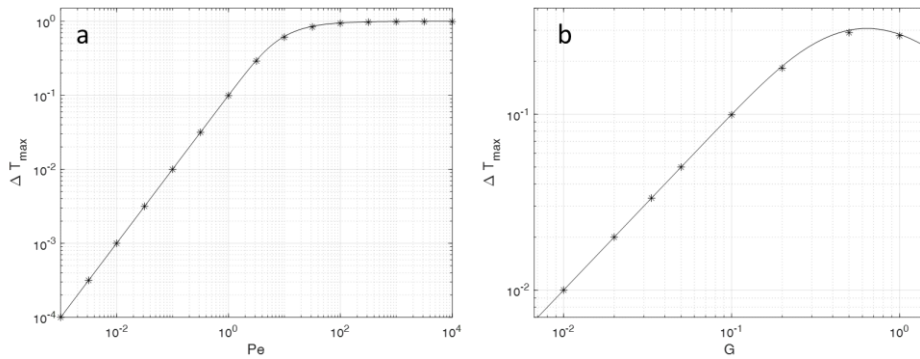
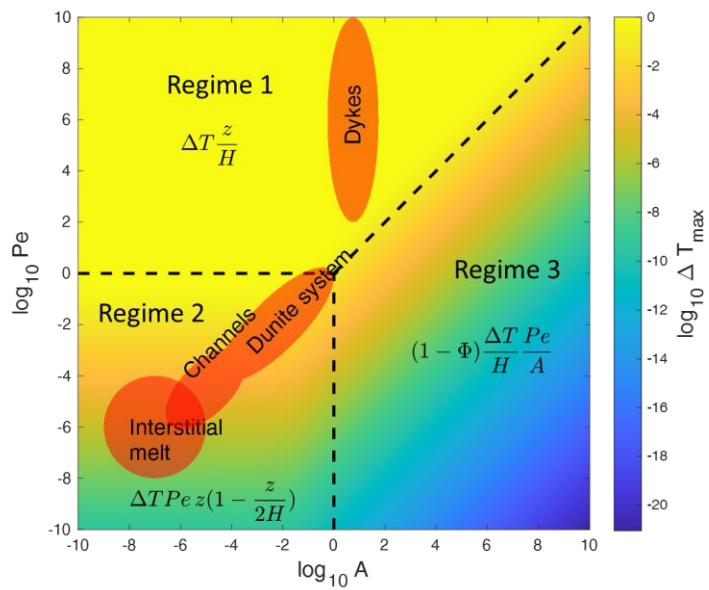


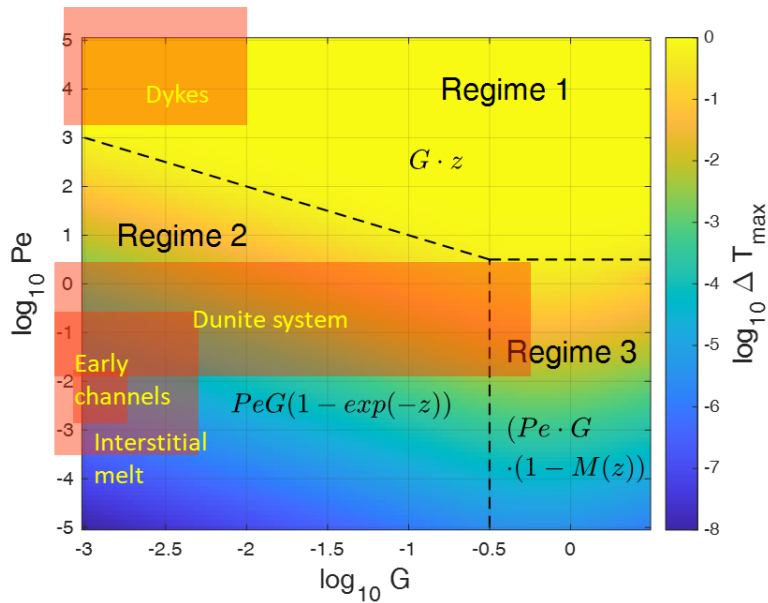
Figure 3. Maximum fluid – solid temperature differences $\Delta T_{\max} T_f - T_s$ of numerical models (asterisks) with different parameters, plotted a) as a function of a) the Peclet number Pe , b) the heat transfer number A , and c) the solid fraction $(1 - \phi)$, for $H = 10$ and $\phi = 0.1$, and b) as a function of the initial thermal gradient G for $Pe = 1$ and $\phi = 0.1$. The solid lines give the analytic solutions.

Formatiert: Schriftfarbe: Rot



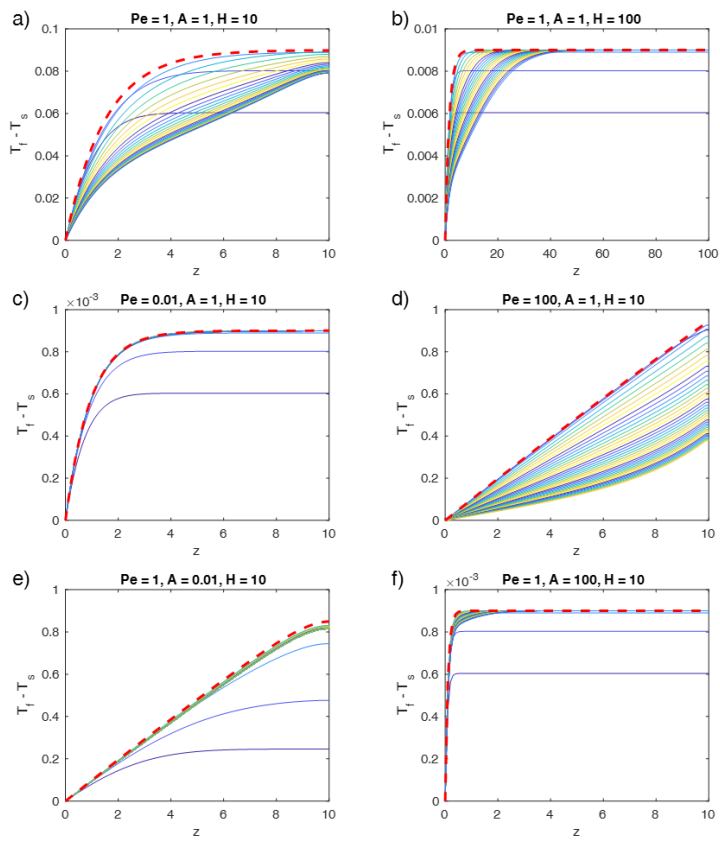
815

820



825 Figure 4. Main regimes of the maximum fluid – solid temperature differences ΔT_{max} due to thermal non-equilibrium obtained by
the analytical solution (equ. 20) and associated limits Eq. 22) in the parameter space of the heat transfer number A and the Peclet
number Pe . The melt fraction ϕ has been assumed as 0.1, and temperature gradient G . The asymptotic limits are indicated by the
formulas, $M(z)$ is given by Eq. (27) with $(1 - M(z))$ increasing non-linearly from about 0 to 0.4 with increasing z . Regime boundaries
are shown as dashed lines. Typical parameter combinations for magmatic settings such as interstitial melts or dykes are indicated
by the orange ellipses/rectangles which extend further to the left, well below $\log_{10} G$ of -3.

Formatiert: Schriftfarbe: Rot



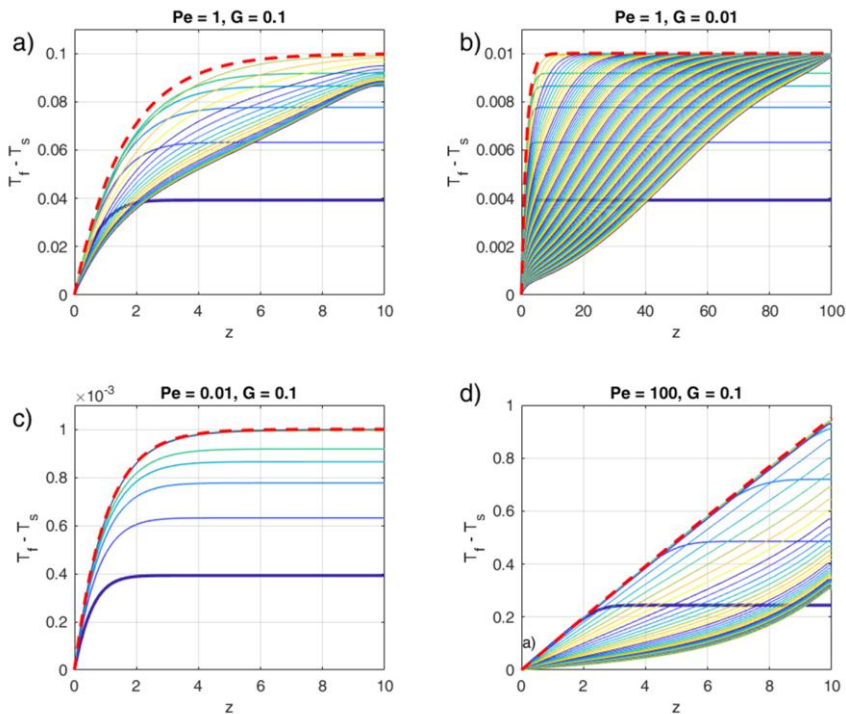


Figure 5. Comparison of depth- and time- dependent numerical solutions with the time – independent analytical solutions for different parameters Pe , A , and HG as indicated in the sub-figure titles. The thin curves in each panel show $(T_f - T_s)$ -profiles for progressive times, the colors are cyclically varied with time from blue to yellow, starting with blue. (bold curve). The bold red dashed curve shows the analytical solution equ. (20Eq. (22)), which represents a very good estimate of the depth-dependent temporal maximum of the temperature difference. In each panel the first 5 curves are plotted at time increments of 0.5 (0.025 for $Pe = 100$), the later curves with 5 (1 for $Pe = 100$). The total non-dimensional times of each panel are: a) – e) 100, d) 15, e) 10, and f) 100. As porosity $\phi = 100$ (500 for $G = 0.01$). The melt fraction was chosen as $\phi_0 = 0.1$ is assumed.

Formatiert: Schriftart: Kursiv

Formatiert: Schriftfarbe: Rot

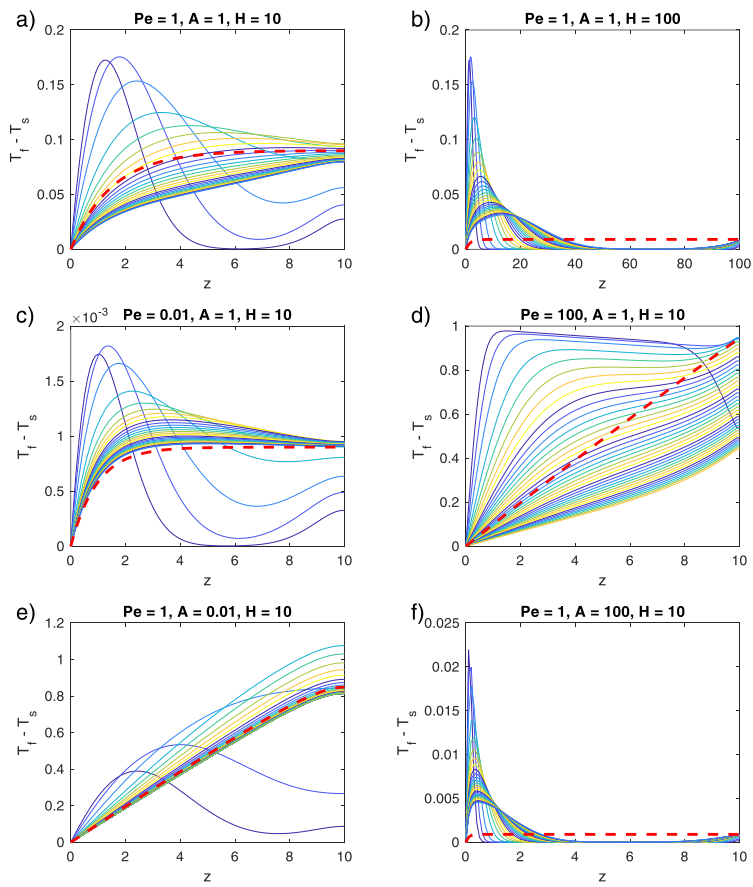
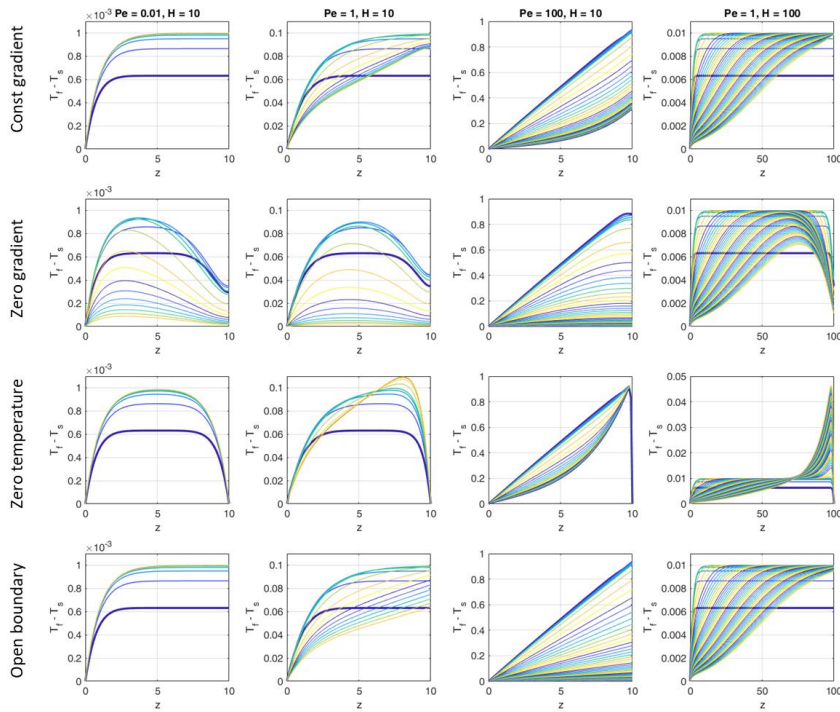


Figure 6.



850 **Figure 6. Temporal evolution of vertical profiles of $(T_f - T_s)$ for models with different Peclet numbers and model heights, i.e. different initial temperature gradients $G = 1/H$. In each panel the curves show $(T_f - T_s)$ -profiles for progressive times, the colors are cyclically varied with time from blue to yellow, starting with blue (bold curve). The first 5 curves of the $Pe < 100$ (respectively $Pe = 100$) models were taken with time increments of 1 (respectively 0.1), the later curves with 10 (respectively 1). The total time was 100 in all models with $H = 10$ and 500 in the models with $H = 100$. In each row the top boundary conditions is assumed as indicated at the left.**

855

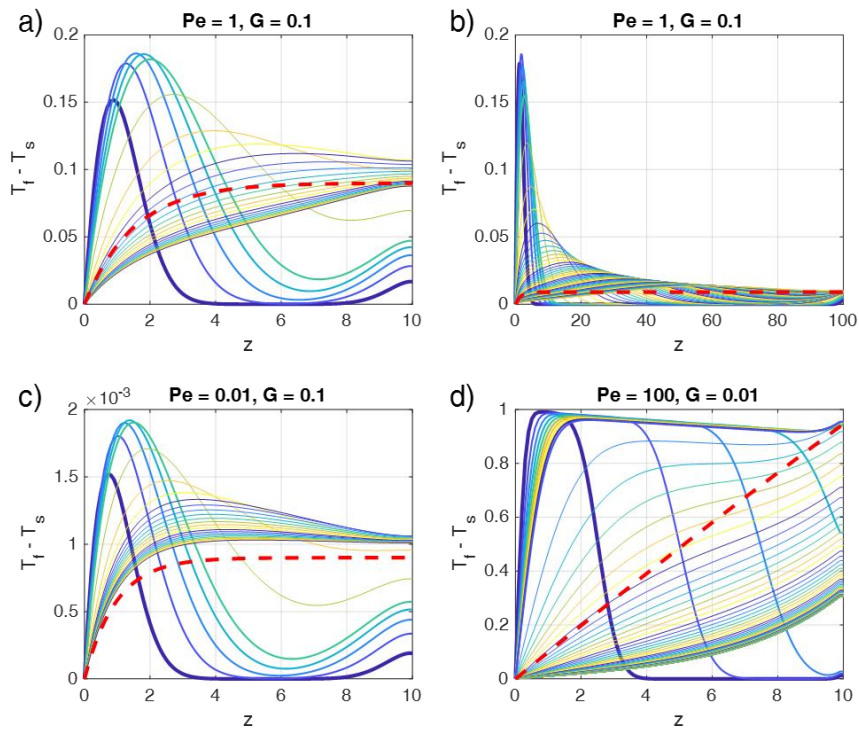
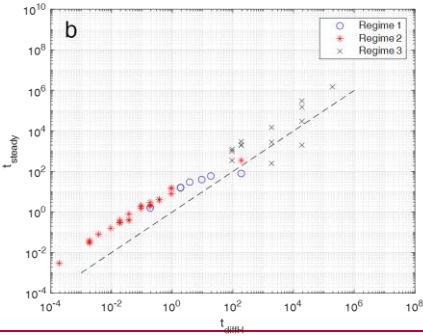
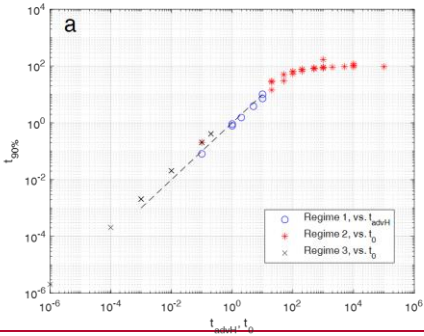


Figure 7. Time- and depth- dependent numerical solutions (thin curves) as in Figure 5 but for step-function initial conditions: $T_f = T_s = 1$ at $z = 0$ and $T_f = T_s = 0$ at $z > 0$ at $t = 0$. **Dashed curves are the time-independent analytical solutions as in Fig. 5.** **The bold dashed red curves are the time-independent analytical solutions as in Fig. 5.** In each panel the curves show $(T_f - T_s)$ -profiles for progressive times, the colors are cyclically varied with time from blue to yellow, starting with blue (bold curve). In each panel the first 5 curves (and later curves, respectively) are plotted at time increments of a) 0.5 (5), b) 1 (10), c) 0.5 (5), and d) 0.025 (1). The total non-dimensional times of each panel are: 100 (500 for $G = 0.01$). As porosity $\phi = 0.1$ is assumed.

Formatiert: Schriftfarbe: Rot



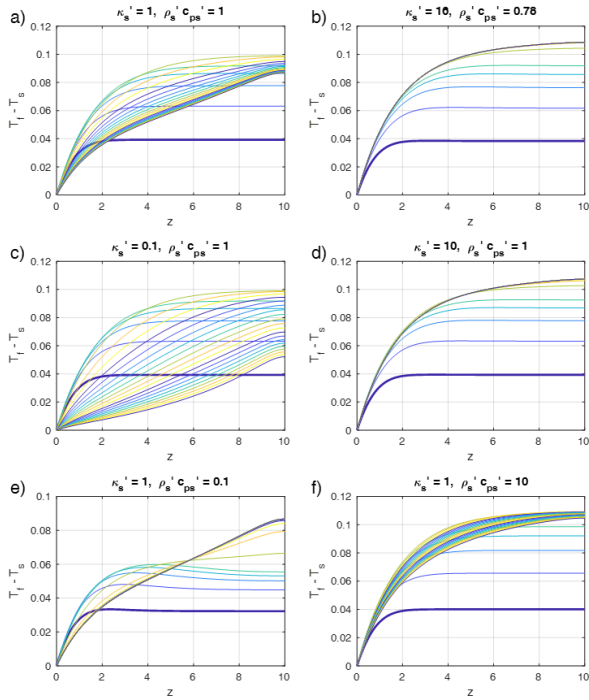


Figure 78. Time- and depth- dependent profiles of the fluid – solid temperature differences as in Fig. 5. a) Reference models (as in Fig. 5a) with $Pe = 1$, $G = 0.1$, $\phi = 0.1$ and equal fluid to solid properties. b) to f) Profiles as in a) but with solid to fluid properties ratios as indicated in the titles of each panel, and $\lambda_{eff}' = 1$. The properties in b) are typical for water in sedimentary rocks. In each panel but b) the first 5 curves were taken with time increments of 0.5, the later curves with 5. In panel b) the first 5 curves were taken with time increments of 0.4875, the later curves with 4.875. The total time was 100 in all models.

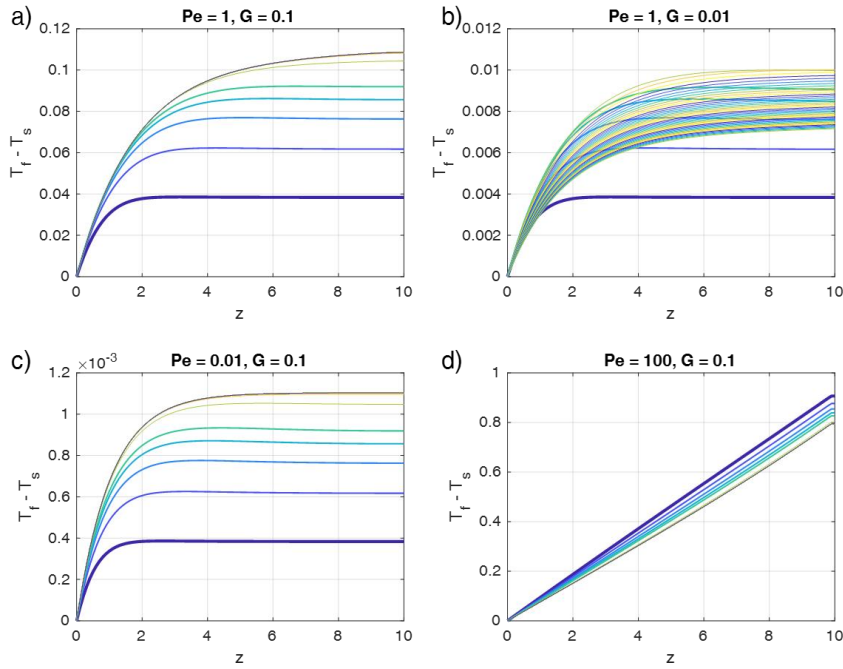
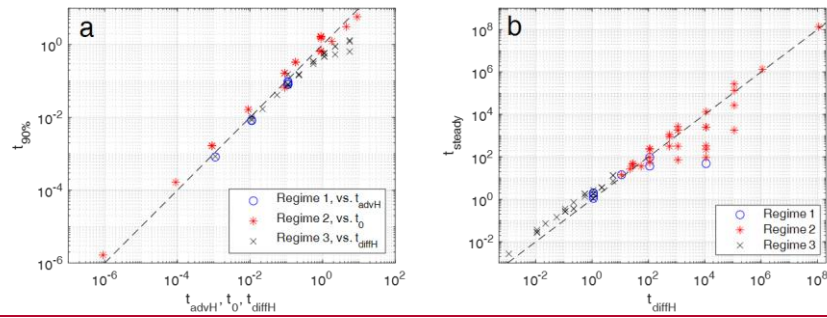


Figure 9. Time- and depth- dependent profiles of the fluid – solid temperature differences as in Fig. 5, but for fluid to solid property ratios typical for water flowing through sedimentary rocks, i.e. $\rho'_s c_{p,s}' = 0.78$, $\kappa'_s = 16$, $\lambda_{eff}' = 1$. Pe and G have been chosen as indicated in the sub-figure titles (as in Fig. 5) and $\phi = 0.1$ was assumed. In each panel the curves show $(T_f - T_s)$ -profiles for progressive times, the colors are cyclically varied with time from blue to yellow, starting with blue (bold curve). The first 5 curves were taken with time increments of 0.4875, the later curves with 4.875. The total time was 100 in all models with $G = 0.1$ and 200 in the models with $G = 0.01$.

885

890



895

900

Figure 10. For evaluating time scales the numerically determined times of models with various parameters Pe , A and H representing the three different regimes 1, 2 and 3 (different symbols) are plotted against characteristic scaling times. a) times Times for reaching 90% of the maximum temperature difference ΔT_{max} are plotted against either the advective time scale t_{advH} based on model height H for regime 1 models, or against the scaling time scale t_0' for regime 2 and 3 models, or against the diffusive time scale t_{diffH} based on the model height H . b) times for reaching steady states are plotted against the characteristic diffusive time scales, t_{diffH} , based on model height H for all 3 regimes. Models close to the dashed line ($y = x$) are in best agreement with the characteristic times. In this Figure a) the Regime 2 times were taken dimensional by setting L_0 multiplying the observed times and κ_0 to the non-dimensional scaling time $t_0' = 1$ to allow for various t_0' s by some arbitrary dimensional times t_0 .

- Formatiert: Schriftart: Kursiv
- Formatiert: Schriftart: Kursiv
- Formatiert: Schriftart: Kursiv, Tiefgestellt
- Formatiert: Schriftart: Kursiv
- Formatiert: Schriftart: Kursiv
- Formatiert: Schriftart: Kursiv, Tiefgestellt
- Formatiert: Schriftart: Kursiv
- Formatiert: Schriftart: Kursiv
- Formatiert: Schriftfarbe: Rot
- Formatiert: Englisch (Vereinigte Staaten)